

## 8 Atmospheric Channel

*Sabino Piazzolla*

### CONTENTS

8.1	Introduction.....	
8.1.1	Statistical Description of Atmospheric Turbulence.....	
8.1.2	Modeling of the Refractive Index Structure Parameter .....	
8.1.3	Propagation in Turbulent Atmosphere.....	
8.1.4	Scintillation Index.....	
8.1.5	Scintillation Statistics.....	
8.1.6	Aperture Averaging Factor.....	
8.1.7	Modeling of Scintillations in Strong Turbulence.....	
8.1.8	Phase Statistics.....	
8.1.9	Beam Effects.....	
8.2	Atmospheric Transmission Loss and Sky Background Noise.....	
8.2.1	Absorption and Scattering.....	
8.2.2	Background Radiation and Sky Radiance.....	
8.3	Conclusions.....	
	References.....	

## **8.1 INTRODUCTION**

When an optical beam propagates in the atmosphere, it can experience attenuation loss of its irradiance and random degradation of the beam quality itself. The first effect is caused by absorption and scattering, operated by molecular constituents and particulates present in the atmosphere. The second effect is related to clear air turbulence (or optical turbulence) that induces (among other things) phase fluctuations of the laser signal, focusing or defocusing effects, local deviations in the direction of electromagnetic propagation, and signal intensity fluctuations at the receiver (also known as signal scintillation). The purpose of this chapter therefore, is to introduce a theoretical basis of the beam propagation characteristics concerning atmospheric absorption loss and clear air turbulence. Particularly, we first introduce a description of the cause of clear air turbulence, a description of scintillation of the optical signal, deterioration of the receiver performance resulting from phase degradation of the signal (due to turbulence), and other beam effects. Finally, we describe the mechanisms that induce atmospheric loss and sky background noise radiance.

### **8.1.1 STATISTICAL DESCRIPTION OF ATMOSPHERIC TURBULENCE**

Clear air turbulence phenomena affect the propagation of an optical beam because the refractive index randomly varies in space and time. Mainly, random variation of the refractive index of air depends on the air mixing due to temperature variation in the atmosphere. In fact, sunlight incident upon the earth's surface causes heating of the earth's surface and the air in its proximity. This sheet of warmed air becomes less dense and rises to combine with the cooler air of the above layers, which causes air temperature to vary randomly (from point to point). Because the atmospheric refractive index depends on air temperature and density, it varies in a

random fashion in space and time, and this variation is the origin of clear air turbulence.

To describe clear air turbulence, one should consider the atmosphere as a fluid that is in continuous flow. A fluid flow at small velocity is first characterized by a smooth laminar phase. In fluid dynamics, a figure of merit of the fluid flow is the Reynolds number ( $Re$ ), which is the ratio between fluid inertial forces and viscous forces [1]:

$$Re = V_c l / \nu_k, \quad (8.1)$$

where,  $V_c$  and  $l$  are the characteristic velocity scale and length given in m/s and m, respectively, and  $\nu_k$  is the kinematics viscosity given in m<sup>2</sup>/s.

The laminar flow of the fluid is stable only when the Reynolds number does not exceed a certain critical value ( $Re \sim 2300$ ). When the Reynolds number exceeds the critical value (e.g., by increasing flow velocity), motion becomes unstable and the flow changes from laminar to a more chaotic, turbulent state. To describe this turbulent state, Kolmogorov developed a theory based on the hypothesis that kinetic energy associated with larger eddies is redistributed without loss to eddies of decreasing size, until they are finally dissipated by viscosity [1]. The structure of the turbulence according to this theory is depicted in Figure 8.1.

The scale of the turbulence can be divided into three ranges: input range, dissipation range, and inertial subrange. The input range, where the energy is injected in the turbulence, is characterized by eddies of size greater than the outer scale of turbulence ( $L_0$ ). Since the turbulence in this range greatly depends on local conditions, there is no mathematical approach capable to describe it. The dissipation range is characterized by eddies of size smaller than the inner scale of turbulence ( $l_0 \ll L_0$ ). In this case, turbulent eddies disappear, the remaining energy is dissipated as heat, and energy loss from eddies (due to viscosity) dominates. The

inertial subrange is at the core to the Kolmogorov' theory, here the turbulence energy is transferred from eddies size  $L_0$  down to eddies of size  $l_0$ , Figure 8.1 [2].

Mathematical description of the turbulent regime is quite complex and is approached with the help of statistics. In this regard, the study by Kolmogorov [1] showed that in a turbulent regime for a statistically homogenous medium, the longitudinal structure function of wind velocity between two observation points,  $\mathbf{R}_1$  and  $\mathbf{R}_2$ , is given in the inertial subrange by

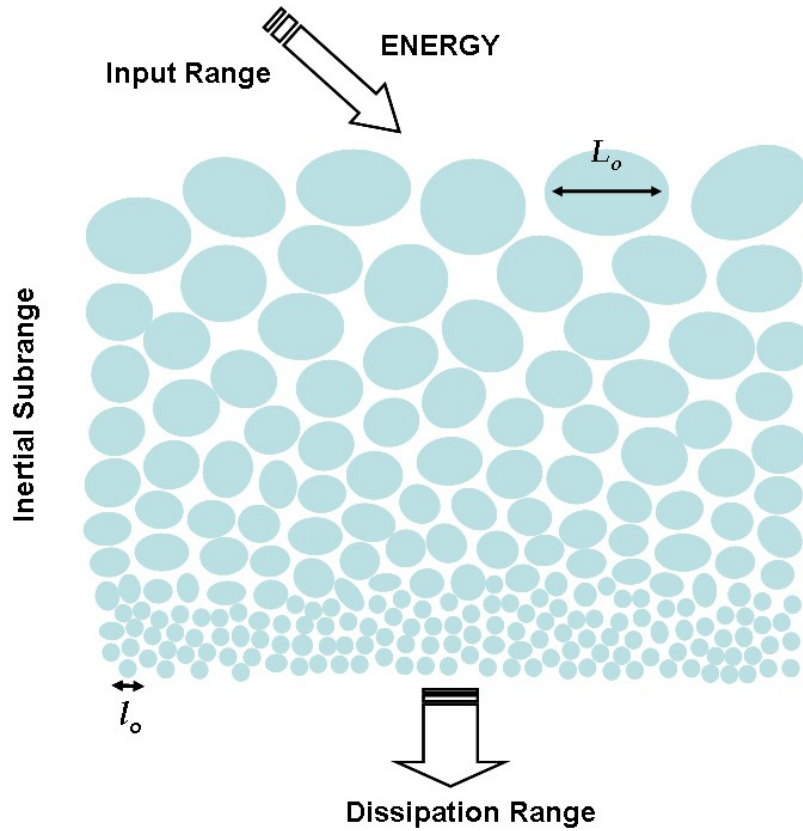


**FIGURE 8.1** Depiction of turbulence regime. The energy is exchanged from larger eddies to smaller ones. In the inertial subrange, the largest eddies have size  $L_0$  and the smallest have size  $l_0$ .

$$\begin{aligned}
 D_v(R) &\equiv D_v(\mathbf{R}_1, \mathbf{R}_2) = \left\langle [v(\mathbf{R}_1) - v(\mathbf{R}_2)]^2 \right\rangle \\
 &= \left\langle [v(\mathbf{R}_1) - v(\mathbf{R}_1 + \mathbf{R})]^2 \right\rangle = C_v^2 R^{2/3}, l_0 \ll R \ll L_0,
 \end{aligned}
 \tag{8.2}$$

where

$\langle \rangle$  is the mean operator

$C_v^2$  is defined as the structure constant of the wind velocity which indicates the strength level of the turbulence

Exponent 2/3 of the distance  $R$  expresses a power law that is true in the inertial subrange

Kolmogorov also derived the three-dimensional power spectrum of wind velocity that is related to  $C_v^2$  and the spatial frequency  $\kappa$  as

$$\Phi_v(\kappa) = 0.033 C_v^2 \kappa^{-11/3}, \quad 1/L_0 \ll \kappa \ll 1/l_0, \quad (8.3)$$

noting that the above spectrum is valid in the inertial subrange.

To extend the Kolmogorov theory to describe the variation of the refractive index in clear air turbulence, one must first describe the refractive index,  $n$ , in terms of observable atmospheric variables. In the optical domain, the refractive index can be described by the following relationship [3]:

$$n - 1 \approx 79 \times 10^{-6} \frac{p}{T}, \quad (8.4)$$

where

$p$  is the atmospheric pressure in mbar

$T$  is the temperature in Kelvin

Again, under the hypothesis of statistically homogenous medium, one can derive the structure function of the refractive index and obtain [3]

$$D_n(n(\mathbf{R})) = \langle [n(\mathbf{R}_1) - n(\mathbf{R}_2)]^2 \rangle = \langle [n(\mathbf{R}_1) - n(\mathbf{R}_1 + \mathbf{R})]^2 \rangle = C_n^2 R^{2/3}; \quad l_0 < R < L_0, \quad (8.5)$$

where the term  $C_n^2$  is the index of refraction structure parameter which indicates the strength of turbulence. At the same time, given Equation 8.4, one can demonstrate that the refractive index structure constant is related to the temperature structure constant  $C_T^2$  as

$$C_n^2 = \left( \frac{78p}{T^2} \times 10^{-6} \right)^2 C_T^2. \quad (8.6)$$

Equation 8.6 indicates that a way to determine the refraction index structure parameter is to measure temperature, pressure, and the temperature spatial fluctuations (to derive  $C_T^2$ ) and finally through Equation 8.6 obtain  $C_n^2$  [4].

### 8.1.2 MODELING OF THE REFRACTIVE INDEX STRUCTURE PARAMETER

As previously mentioned, the refractive index structure parameter is the most significant parameter that determines the turbulence strength. Clearly,  $C_n^2$  depends (among different variables) on the geographical location, altitude, and time of day. Different locations can have different characteristics of temperature distribution (e.g., tropical location vs. temperate location) that are reflected on the values assumed by  $C_n^2$ . Close to ground, there is the largest gradient of temperature associated with the largest values of atmospheric pressure (and air

density), therefore, one should expect larger values of  $C_n^2$  at sea level. As the altitude increases, the temperature gradient decreases and so the air density (and atmospheric pressure) with the result of smaller values of  $C_n^2$ .

Considering the temperature dynamic during the day, one should expect turbulence to be stronger around noon. Conversely, at sunset and dawn, due to a form of thermal equilibrium along the atmosphere vertical profile, one should expect  $C_n^2$  to have lower values.

In applications that envision a horizontal path even over a reasonably long distance, one can assume  $C_n^2$  to be practically constant. Typical value of  $C_n^2$  for a weak turbulence at ground level can be as little as  $10^{-17} \text{ m}^{-3/2}$ , while for a strong turbulence it can be up to  $10^{-13} \text{ m}^{-3/2}$  or larger. If we instead consider application from ground to space, or more generally, along a slant path,  $C_n^2$  must vary due to the different temperature gradient, air pressure, and density along the altitude. Modeling and determining the profile of  $C_n^2$  with altitude is not a simple task. In fact, it is not easy to capture properly the variations of  $C_n^2$  measured usually with thermosondes. Generally, experimental data of  $C_n^2$  are not readily available. However, a number of parametric models have been formulated to describe the  $C_n^2(h)$  profile and among those, one of the more used models is the Hufnagel-Valley [5] given by

$$C_n^2(h) = 0.00594 (v/27)^2 (10^{-5}h)^{10} \exp(-h/1000) + 2.7 \times 10^{-16} \exp(-h/1500) + A_0 \exp(-h/100), \quad (8.7)$$

where

$h$  is the altitude in m

$v$  and  $A_0$  are parameters to be set by the user

Particularly,  $A_0$  (dimensionally  $\text{m}^{-2/3}$ ) defines the turbulence strength at the ground level, while  $v$  is the rms wind speed at high altitude (dimensionally  $\text{m/s}$ ). The Hufnagel-Valley model, therefore, allows an easy modification of the  $C_n^2(h)$  profile by changing values of the parameters  $A_0$  and  $v$ . Particularly, for an  $A_0 = 1.7 \times 10^{-14} \text{ m}^{-2/3}$  and  $v = 21 \text{ m/s}$ , the Hufnagel-Valley is commonly termed as HV5/7 because it generates the conditions for an atmospheric coherence length of 5 cm and an isoplanatic angle of 7  $\mu\text{rad}$  (definitions of these last two terms will be introduced later in this chapter) at a wavelength of 500 nm.

Beside the Hufnagel-Valley, a number of other empirical/experimental models of the  $C_n^2(h)$  are available. Again, great care must be applied when one uses these models because (beside their daytime variability) they are most accurate when applied to describe  $C_n^2(h)$  in the geographical location where the measurements were made. For instance the CLEAR 1 model [3] is pertinent to the New Mexico desert, and describes the nighttime  $C_n^2(h)$  profile for altitude as  $1.23 < h < 30 \text{ km}$  as

$$\begin{aligned} C_n^2(h) &= 10^{-17.025 - 4.3507h + 0.8141h^2} \text{ for } 1.23 < h \leq 2.13 \text{ km} \\ C_n^2(h) &= 10^{-16.2897 + 0.0335h - 0.01341h^2} \text{ for } 2.13 < h \leq 10.34 \text{ km} \\ C_n^2(h) &= 10^{-17.0577 - 0.0449h - 0.00051h^2 + 0.6181 \exp(-0.5(h - 15.5617)/12.0173)} \text{ for } 10.34 < h \leq 30 \text{ km} \end{aligned} \quad (8.8)$$

where altitude  $h$  is expressed in km, while above 30 km, the refractive index structure constant is supposed to be zero. The CLEAR 1 model was obtained by averaging and statistically interpolating a number of thermosonde observation measurements obtained over a large number of meteorological conditions. The lower limit of 1.23 km of ground elevation is



pertinent to the altitude of the New Mexico region where such measurements took place [3]. Another  $C_n^2(h)$  model is Submarine Laser Communication (SLC) that was developed for the AMOS observatory in Maui, Hawaii. The daytime profile of  $C_n^2(h)$  according to SLC model is given by [2]:

$$\begin{aligned}
C_n^2(h) &= 8.40 \times 10^{-15} && \text{for } h \leq 18.5\text{m} \\
C_n^2(h) &= (3.13 \times 10^{-13})/h && \text{for } 18.5 < h \leq 240\text{m} \\
C_n^2(h) &= 1.3 \times 10^{-15} && \text{for } 240 < h \leq 880\text{m} \\
C_n^2(h) &= 8.87 \times 10^{-7}/h^3 && \text{for } 880 < h \leq 7,200\text{m} \\
C_n^2(h) &= 2.0 \times 10^{-16}/h^{1/2} && \text{for } 7,200 < h \leq 20,000\text{m}
\end{aligned} \tag{8.9}$$

A graphic comparison of the three different parametric models of  $C_n^2(h)$  (HV5/7, CLEAR 1, and SLC Day) are plotted in Figure 8.2. Again, a careful choice of  $C_n^2(h)$  model that must be taken when used to calculate the different figures of merit describing propagation of a beam in a turbulent atmosphere. For instance, variation of the rms wind velocity in the Hufnagel-Valley will lead to a different profile of  $C_n^2(h)$  at higher levels of the atmosphere, while variation of daytime and nighttime of  $C_n^2(h)$  can be described by a multiplier of the parametric model selected. In any case, great care is suggested when adopting a model or another (including experimental measurements) because the large dynamics of atmospheric conditions can lead to a great variation of the  $C_n^2(h)$  profile.

As analogously expressed for the wind velocity in Equation 8.2, the Kolmogorov three-dimensional spectrum of the refractive index spectrum is

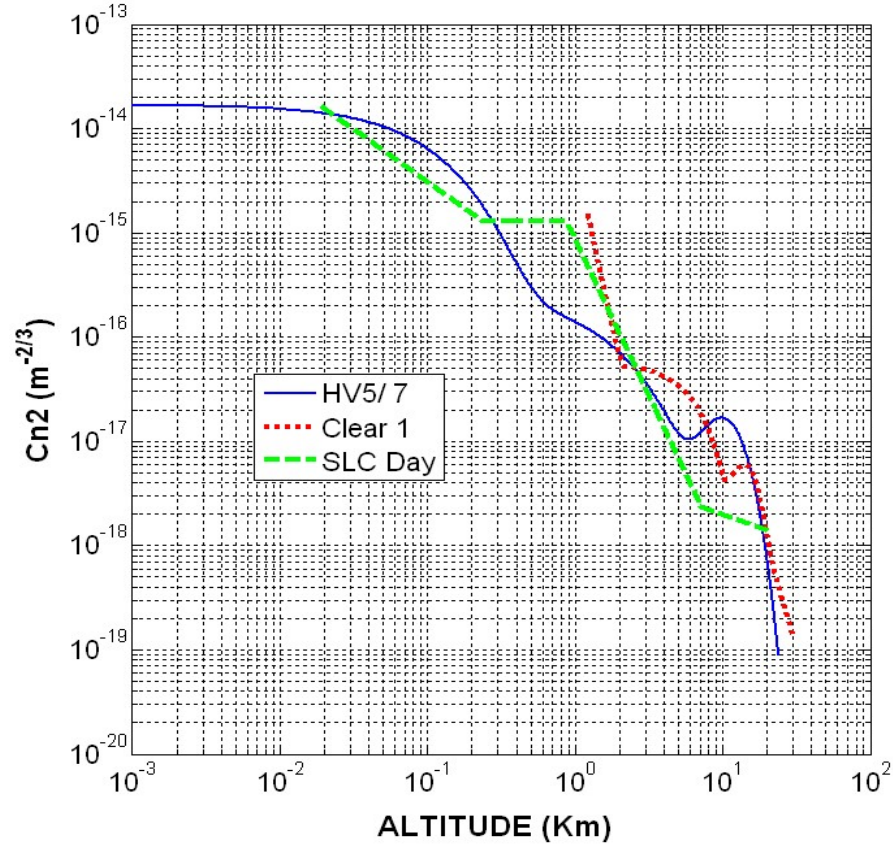


**FIGURE 8.2 Comparison of three models of atmospheric profile of the structure constant of the refractive index. HV5/7, CLEAR 1, and SLC Day are plotted. Notice that, due to geographical specificity of each model, not all models extend to the sea level.**

$$\Phi_n(\kappa, h) = 0.033 C_n^2(h) \kappa^{-11/3}, \quad 1/L_0 \ll \kappa \ll 1/l_0. \quad (8.10)$$

Here, the spectrum depends on the altitude  $h$ , and (of course) has the limitation to be applicable only in the inertial subrange [6]. A modification to the Kolmogorov spectrum is the so-called modified von Karman spectrum [4] which is given by

$$\Phi_n(\kappa, h) = 0.033 C_n^2(h) \frac{\exp(-\kappa^2 / \kappa_m^2)}{(\kappa^2 + \kappa_0^2)^{11/6}}, 0 \leq \kappa < \infty, \quad (8.11)$$

where

$$\kappa_m = 5.92/l_0$$

$$\kappa_0 = 1/L_0.$$

The modified von Karman spectrum (as other spectrum available in literature of the refractive index) has the same behavior of the Kolmogorov spectrum in the inertial sub-range of spectrum, but it is analytically easier to handle outside the inertial sub-range having the singularity of the Kolmogorov spectrum at  $\kappa = 0$  removed.

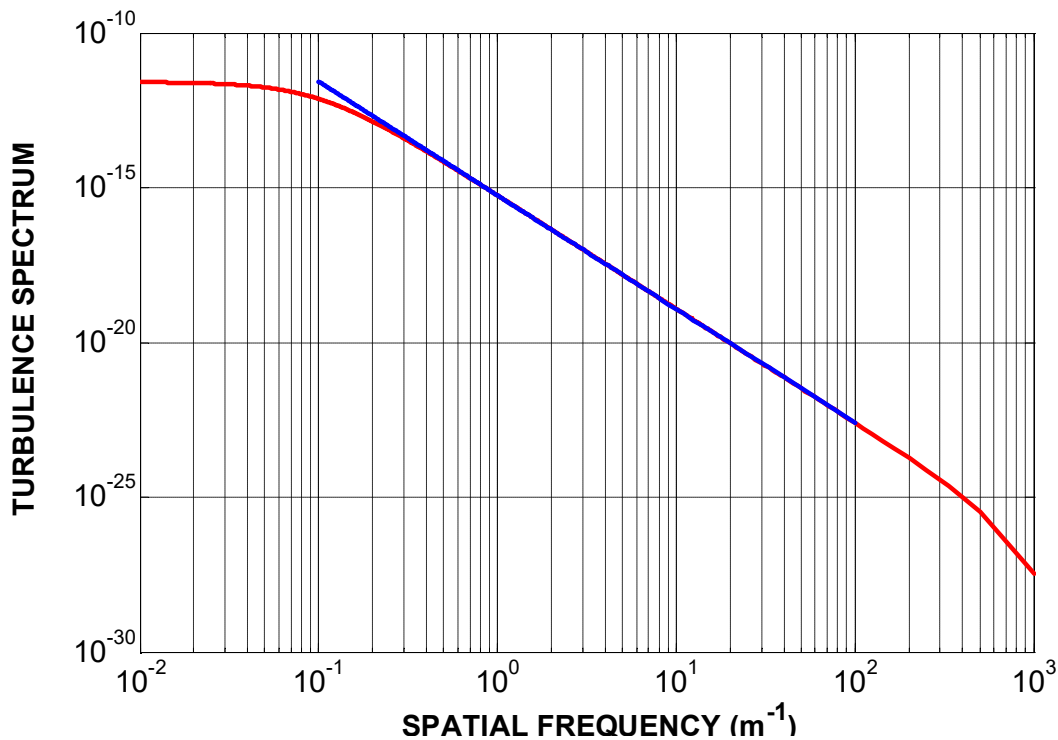


**FIGURE 8.3** Comparison between the Kolmogorov's turbulence spectrum (solid line) and the von Karman's turbulence spectrum (dashed line). Notice that in the figure  $C_n^2 = 10^{-13}(\text{m}^{-2/3})$  while the actual subinertial range is between 10 cm and 10 m.

### 8.1.3 PROPAGATION IN TURBULENT ATMOSPHERE

To describe the propagation of a monochromatic electromagnetic wave  $\mathbf{E}$  in clear air turbulence, one should start (as usual) from Maxwell's equations:

$$\nabla^2 \mathbf{E} + k^2 n^2 \mathbf{E} + 2\nabla[\mathbf{E} \cdot \nabla \log n] = 0, \quad (8.12)$$

where

$\mathbf{E}$  is the vector electric field

$n$  is the (random) refractive index

$k = 2\pi/\lambda$  is the propagation constant

Laplacian operator is described by  $\nabla^2 = \partial^2/\partial x^2 + \partial^2/\partial y^2 + \partial^2/\partial z^2$

Neglecting depolarization of the wave, and under the condition that the wavelength  $\lambda$  is much smaller than the scale of turbulence, one obtains that the vector wave equation of Equation 8.12 can be rewritten in the scalar form:

$$\nabla^2 E + k^2 n^2 E = 0, \quad (8.13)$$

where  $E$  is a scalar component of the electric field.

A number of approaches have been considered to solve the above stochastic differential equation (notice, again, that  $n$  is here a random term). Among these, one of the best known is the Rytov method [7], whose solution holds interesting and practical consequences for the characterization of the wave propagation in random media.

According to the Rytov method, one first describes the scalar field as the complex

exponential form

$$E = \exp(\psi), \quad (8.14)$$

with  $\psi = \log(E)$ . Then, rewriting the scalar Maxwell equation in terms of the exponential term  $\psi$ , one gets the Riccati equation:

$$\nabla^2 \psi + \nabla \psi \cdot \nabla \psi + k^2 n^2 = 0. \quad (8.15)$$

A closed solution of the above equation is not obtainable. However, using the perturbation expansion of the electric field one can write

$$E = \exp(\psi_0 + \psi_1) \quad (8.16)$$

where  $E_0 = \exp(\psi_0)$  is the incident field,  $\psi_1$  the field perturbation related to the first order scattering of the field.

Of course,  $E_0$  is the solution of the Maxwell's equation without perturbation. As a consequence of Equations 8.14 and 8.16, one can write the exponential turbulence term as

$$\psi_1 = \psi - \psi_0 = \log\left(\frac{|E|}{|E_0|}\right) + j(\phi - \phi_0) = \chi + jS \quad (8.17)$$

where

$\chi$  is the field log-amplitude

$S$  is the field phase fluctuations

Demonstration of the solution of the Riccati stochastic differential equation using Rytov method is not shown here because it goes beyond the scope of this chapter [3]. However, understanding the main results of the Rytov method has great implications in the definition of the most meaningful figure of merits of the problem. From the solution of the Riccati equation, one finds that the lognormal amplitude  $\chi$  and the phase term  $S$  depends on the variation of the random refraction index along propagation path. Because of the integration of the random effects along the propagation path, one can consider that overall random perturbation implies a normal distribution of  $\chi$  and  $S$ , with the consequence that both, the wave amplitude [proportional to  $\exp(\chi)$ ] and wave intensity [proportional to  $\exp(2\chi)$ ] of the wave have lognormal distribution, a conclusion that has also been proved experimentally correct for weak turbulence [3].

#### 8.1.4 SCINTILLATION INDEX

One of the effects of clear air turbulence is the fluctuation of the signal irradiance. In nature such irradiance fluctuation is also manifested in the twinkling of a star seen with the naked eye. The scintillation index,  $\sigma_I^2$ , describes such intensity fluctuation (otherwise known as scintillation) as the normalized variance of the intensity fluctuations given by

$$\sigma_I^2 = \frac{\langle (I - \langle I \rangle)^2 \rangle}{\langle I \rangle^2} = \frac{\langle I^2 \rangle}{\langle I \rangle^2} - 1 \quad (8.18)$$

where  $I = |E|^2$  is the signal irradiance (or intensity).

Using results from the Rytov method, one can express the scintillation index in terms of the

variance of the field log-amplitude,  $\sigma_\chi^2$ , as [3]

$$\sigma_I^2 = \exp(4\sigma_\chi^2) - 1 \approx 4\sigma_\chi^2 \quad (8.19)$$

where the right-hand side approximation is valid for the condition of weak turbulence mathematically corresponding to  $4\sigma_\chi^2 < 1$ . Expressions of lognormal field amplitude variance depend on (among other things) the nature of the electromagnetic wave traveling in the turbulence and on the link geometry. Concerning the geometry of the optical link, one can generalize that the case studies are divided into downlink, uplink, and horizontal path. According to the Rytov method, one can write the downlink lognormal variance for a plane wave as [3]

$$\sigma_\chi^2 = 0.56k^{7/6} \sec(\theta)^{11/6} \int_{h_0}^{h_0+L} C_n^2(h)(h-h_0)^{5/6} dh, \quad (8.20)$$

where Equation 8.20 describes a slant path between the two altitudes at  $h_0 + L$  (source location) and  $h_0$  (receiver location) with an angle from the zenith  $\theta$  for total path length  $L/\cos(\theta)$ .

For a spherical wave, the variance of the lognormal field amplitude is instead

$$\sigma_x^2 = 0.56k^{7/6} \sec(\theta)^{11/6} \int_{h_0}^{h_0+L} C_n^2(h)(h-h_0)^{5/6} (1-(h-h_0)/L)^{5/6} dh. \quad (8.21)$$

Concerning the uplink, the expression of the variance of the lognormal amplitude for a plane wave is

$$\sigma_x^2 = 0.56k^{7/6} \sec(\theta)^{11/6} \int_{h_0}^{h_0+L} C_n^2(h)(L+h_0-h)^{5/6} dh, \quad (8.22)$$

for a spherical wave instead, one can get

$$\sigma_x^2 = 0.56k^{7/6} \sec(\theta)^{11/6} \int_{h_0}^{h_0+L} C_n^2(h)(L+h_0-h)^{5/6} (1-(L+h_0-h)/L)^{5/6} dh. \quad (8.23)$$

The horizontal path is characterized by a constant  $C_n^2$ , the variance of the log-amplitude of the field for a plane wave over a path  $L$  will then be

$$\sigma_\chi^2 = 0.307k^{7/6} C_n^2 L^{1/6}, \quad (8.24)$$

for a spherical wave over a path  $L$

$$\sigma_\chi^2 = 0.124k^{7/6} C_n^2 L^{1/6}. \quad (8.25)$$

Other closed form expressions of  $\sigma_\chi^2$  can be obtained for the propagation of a Gaussian beam [2]. Such expressions, however, can have much more complicated mathematical descriptions than those presented in this section.

### 8.1.5 SCINTILLATION STATISTICS

As indicated in Section 8.13, the lognormal amplitude can be statistically described by a Gaussian distribution. As a result of the Rytov method, for weak turbulence of the irradiance,



fluctuation of a propagating beam can be described by a lognormal distribution. Therefore, one can derive that the irradiance probability density function (PDF) is given by

$$p_I(I) = \frac{1}{\sqrt{2\pi}I\sigma_I} \exp \left\{ -\frac{\left[ \ln \left( \frac{I}{\langle I \rangle} \right) + \frac{1}{2} \sigma_I^2 \right]^2}{2\sigma_I^2} \right\} \quad (8.26)$$

where  $\langle I \rangle$  is the average irradiance, Figure 8.4.

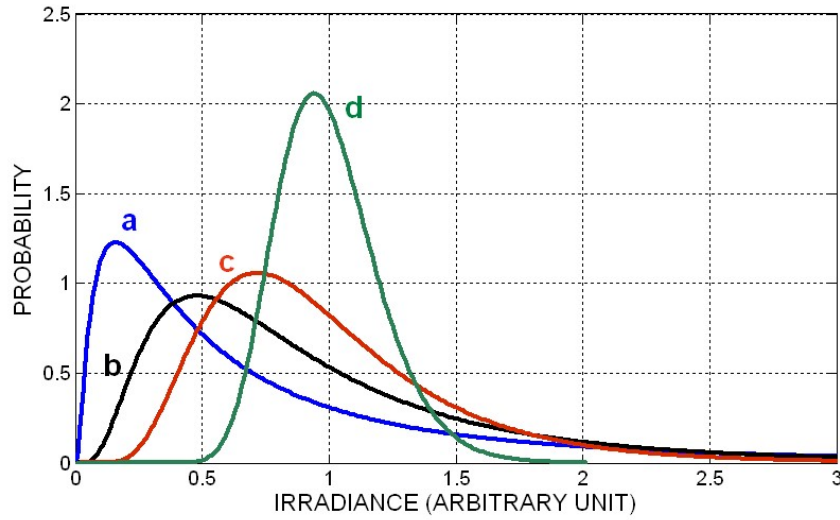


**FIGURE 8.4 Irradiance PDF for a weak turbulence for different values of variance of the lognormal field amplitude: (a)  $\sigma_\chi^2 = 0.2$ ; (b)  $\sigma_\chi^2 = 0.1$ ; (c)  $\sigma_\chi^2 = 0.05$ ; and (d)  $\sigma_\chi^2 = 0.025$ .**

**The average irradiance here is  $\langle I \rangle = 1$  in arbitrary unit.**

Once defined the PDFs for weak turbulence, one can describe the statistics of the signal fluctuations above and below the nominal average irradiance  $\langle I \rangle$ . During a link design, those fluctuations below the average irradiance manifest themselves as dynamical signal loss (or

signal fade), and it is of concern for system engineers to quantify fade probability or (in other terms) the amount of time that the received signal is below a determined fade limit. If one defines a lower limit of the irradiance at the receiver as  $I_F$ , the signal fade threshold  $F_T$ , in dB is

$$F_T = 10 \log_{10} \left( \frac{\langle I \rangle}{I_F} \right), \quad (8.27)$$

where the fade threshold  $F_T$  can be considered an additional loss that can be tolerated by the system. Using Equation 8.27, one can calculate the probability that the signal will be below  $I_F$  (or to have an additional loss larger than  $F_T$ ) as

$$P_F = \int_0^{I_F} p_I(I) dI = \int_0^{I_F} \frac{1}{\sqrt{2\pi} I \sigma_I} \exp \left\{ - \frac{\left[ \ln \left( \frac{I}{\langle I \rangle} \right) + \frac{1}{2} \sigma_I^2 \right]^2}{2 \sigma_I^2} \right\} dI = \frac{1}{2} \left\{ 1 + \operatorname{erf} \left( \frac{\sigma_I^2 - 0.46 F_T}{2 \sqrt{2} \sigma_I^2} \right) \right\} \quad (8.28)$$

Scintillation of the irradiance affects the overall system performance as well as degrades the bit error rate (BER) of the receiver. As an example, one can consider the direct detection of a signal modulated on–off keying. In Chapter 2, it was shown that the BER in the absence of turbulence is

$$\operatorname{BER}(Q) = \frac{1}{2} \operatorname{erfc} \left( \frac{Q}{\sqrt{2}} \right). \quad (8.29)$$

where  $Q$  is related to the detector current as

$$Q(I) = \frac{R_s A_R I L_T}{\sqrt{\sigma_1^2} + \sqrt{\sigma_0^2}}, \quad (8.30)$$

where

$R_s A_R I L_T$  is the current generated at the receiver during the high state (usually) corresponding to the digit “1”

$R_s$  is the detector responsivity

$I$  is the signal irradiance when the digit “1” is transmitted

$A_R$  is the entrance pupil area

$L_T$  is the optical system loss

$\sigma_1^2$  is the current noise power during the high signal state

$\sigma_0^2$  is the current noise power during the low state

In the presence of atmospheric turbulence, the BER is calculated by averaging it over the intensity PDF, which is given by

$$\langle \text{BER} \rangle = \int_0^\infty p_1(I) \text{BER}[Q(I)] dI. \quad (8.31)$$

### 8.1.6 APERTURE AVERAGING FACTOR

So far we have described the irradiance fluctuation and scintillation index experienced by a point collecting aperture. However, as the collecting aperture of a receiver system increases,

the receiver experiences a reduction of the fluctuation of total received power. This fluctuation reduction is related to the averaging of the nonuniform irradiance integrated by the collecting aperture, referred to as aperture averaging [8]. To quantify the aperture averaging, it is usually introduced by the concept of averaging aperture factor,  $A_v$ , defined as the ratio between  $\sigma_1^2(D)$  (the normalized flux variance of the collection aperture of diameter  $D$ ) over the scintillation index

$$A_v = \frac{\sigma_1^2(D)}{\sigma_1^2} < 1. \quad (8.32)$$

In Ref. [9], the aperture averaging factor is written in terms of the covariance of the irradiance ( $C_I(x)$ ) and the optical transfer function of the circular aperture ( $M(x)$ ) as

$$A_v = \frac{1}{8} \int_0^1 \frac{C_I(xD)}{C_I(0)} M(x) x dx. \quad (8.33)$$

Finding an exact analytical solution to the above is a very challenging problem. However, for the case of a link from space to Earth (downlink), an approximated and very practical solution to Equation 8.33 has been presented in Ref. [10] for weak turbulence for both plane and spherical waves where the aperture averaging factor is expressed by the formula

$$A_v = \left[ 1 + 1.1 \left( \frac{D^2}{\lambda h_s \cos(\theta)} \right)^{7/6} \right]^{-1} \quad (8.34)$$

where

$\theta$  is the angle from the zenith for slant path

$h_s$  is a scale height of the turbulence defined as

$$h_s = \left[ \frac{\int_{h_0}^{h_0+L} C_n^2(h)(h-h_0)^2 (1-(h-h_0)/L)^{-1/3} dh}{\int_{h_0}^{h_0+L} C_n^2(h)(h-h_0)^2 (1-(h-h_0)/L)^{5/6} dh} \right]^{6/7} \quad (8.35)$$

where the above equation is valid for a spherical wave, and  $L$  is the difference in altitude between the source (at  $h_0 + L$ ) and the receiver (at  $h_0$ ). At the same time, one can derive the scale height of the turbulence for a plane wave as

$$h_s = \left[ \frac{\int_{h_0}^{h_0+L} C_n^2(h)(h-h_0)^2 dh}{\int_{h_0}^{h_0+L} C_n^2(h)(h-h_0)^{5/6} dh} \right]^{6/7} . \quad (8.36)$$

In the instance of a horizontal path with constant  $C_n^2$  over a link distance  $L$ , the aperture averaging factor for a plane wave is [2]

$$A_v = \left[ 1 + 1.06 \left( \frac{kD^2}{4L} \right) \right]^{-7/6} , \quad (8.37)$$

while for spherical waves it holds that [2]

$$A_v = \left[ 1 + 0.33 \left( \frac{kD^2}{4L} \right) \right]^{-7/6} \quad (8.38)$$

### 8.1.7 MODELING OF SCINTILLATIONS IN STRONG TURBULENCE

Scintillation statistics and theory so far described apply to weak turbulence. As the strength of the turbulence increases, reaching the condition of strong turbulence ( $4\sigma_\chi^2 > 1$ ), the lognormal statistical characterization of the irradiance PDF fails to adequately represent the process [11]. However, a number of other statistical models have been suggested in the literature to describe scintillation statistics in a regime of strong turbulence. For instance, one of the first models used for this purpose was the  $K$  distribution [12, 13]. Later, statistical models were presented that were based on the lognormal Rician distribution, which presented the computational and numerical problem of not being available in closed form [14, 15]. However, it must be pointed out that both, the  $K$  distribution and the lognormal Rician distribution cannot easily relate their mathematical parameters with the observables of the atmospheric turbulence, which limits their applicability and utilization. Alternatively, the gamma-gamma distribution is quite successfully used to describe scintillation statistics for weak and strong turbulence conditions [16]. While still mathematically complex, the gamma-gamma distribution can be expressed in closed form (unlike the lognormal Rician) and can relate its main parameters to the scintillation conditions (scintillation index, large-scale scintillation, etc.). Particularly, for a downlink signal the PDF of the fluctuation of the normalized irradiance ( $\hat{I} = \frac{I}{\langle I \rangle}$ ) is expressed by the gamma-gamma distribution as [2]

$$p(\hat{I}) = \frac{2(\alpha\beta)^{(\alpha+\beta)/2} (\hat{I})^{(\alpha+\beta)/2-1} K_{\alpha-\beta}(2\sqrt{\alpha\beta\hat{I}})}{\Gamma(\alpha)\Gamma(\beta)} \quad (8.39)$$

where  $K(\cdot)$  is a modified Bessel function of second kind,  $\alpha$  and  $\beta$  are related to the scintillation index as

$$\sigma_I^2 = \frac{1}{\alpha} + \frac{1}{\beta} + \frac{1}{\beta\alpha} \quad (8.40)$$

The scintillation index in Eq. 8.40 is for downlink beam experiencing weak to strong turbulence conditions, and it calculated as [2]

$$\sigma_I^2 = \exp\left(\frac{0.49\sigma_R^2}{(1+1.11\sigma_R^{12/5})^{7/6}} + \frac{0.51\sigma_R^2}{(1+0.69\sigma_R^{12/5})^{5/6}}\right) - 1 \quad (8.41)$$

where  $\sigma_R^2 = 4\sigma_\chi^2$ , with the Rytov's variance as in Eq. 8.24, with  $0 \leq \sigma_\chi^2 \leq \infty$ .

In terms, the parameters  $\alpha$  and  $\beta$  are expressed as

$$\alpha = \left\{ \exp\left(\frac{0.49\sigma_R^2}{(1+1.11\sigma_R^{12/5})^{7/6}}\right) - 1 \right\}^{-1} \quad (8.42)$$

$$\beta = \left\{ \exp\left(\frac{0.51\sigma_R^2}{(1+1.11\sigma_R^{12/5})^{5/6}}\right) - 1 \right\}^{-1} \quad (8.43)$$

As an alternative to analytical models, wave-optics simulation has largely been used with success to simulate and study the effects of clear air turbulence on a propagating optical beam [17]. Compared to analytical methods, wave-optics numerically simulates the propagation in the time domain of a two-dimensional wave front of an electric field sampled in a spatial grid described by a mesh of  $\mathbf{N} \times \mathbf{N}$  elements over an area of interest [18]. In a wave-optics simulation, the atmosphere along the direction of propagation is divided into a cascade of  $\mathbf{M}$  layers [17]. In the case of laser beam propagation (e.g., from transmitter to receiver), the propagation of the two-dimensional wave front of the electric field from the beginning of one layer to the beginning of the next layer takes place in two steps. In the first step, the phase of the spatially sampled electric field is modulated by a random phase screen [19] whose strength is determined by the  $C_n^2$  in the layer. This phase screen describes the phase aberrations

experienced by the propagating wave that are induced by the atmospheric turbulence within the layer (described in Section 8.1.5). In the next step, the electrical field is propagated to the beginning of the next layer using fast-Fourier-transform techniques [17]. The propagation process is repeated through the cascade of atmospheric layers until the wave reaches the collection aperture of the receiver where the wave intensity is integrated over the aperture surface. This procedure describes the propagation of the wave in one single realization at the initial time ( $t_1$ ), while wave-optics allows a simulation over an extended time period. Therefore, to simulate the propagation over the next time interval, the process is updated to the next time step  $t_1 + \Delta t$ , in which the phase screen of each layer experiences a spatial shift as  $v_T \Delta t$ , where  $v_T$  is the transversal component of the wind speed at the corresponding layer. Once the phase screens are updated, the wave propagation through the  $\mathbf{M}$  layers is repeated. Then, the wave intensity is (again) collected at the receiver at the time  $t_1 + \Delta t$ . The algorithm (phase screen update and propagation) is repeated  $n$  times until the simulation reaches its final target time ( $t_1 + n\Delta t$ ) and the simulation output time evolution of process is provided.

Wave-optics simulations are extensively used, not only in simulating intensity scintillation dynamics, but also in a number of applications of adaptive optics, optical tracking, and laser communications. Finally, one must also consider the not trivial advantage over analytical approaches that wave-optics simulation techniques can be used regardless of the turbulence strength (weak or strong), nature, and profile.

### 8.1.8 PHASE STATISTICS

In clear air turbulence, the random variation of the atmospheric refractive index induces a random degradation of the phase of wave front of a propagating electromagnetic wave. Again, to describe the random variation of the phase ( $\phi$ ) of an electromagnetic wave, one can use the



phase structure function between two points ( $\mathbf{R}_1$  and  $\mathbf{R}_2 = \mathbf{R}_1 + \mathbf{R}$ ) given by [3]

$$D_\phi(\mathbf{R}) = \left\langle [\phi(\mathbf{R}_1) - \phi(\mathbf{R}_1 + \mathbf{R})]^2 \right\rangle = 2.914k^2 \sec(\theta) \mathbf{R}^{5/3} \int_{h_0}^{h_0+L} C_n^2(h) dh, \quad (8.44)$$

where the above equation relates to a generic plane wave traveling between the altitudes  $h_0 + L$  and  $h_0$  with an inclination angle from the zenith of  $\theta$ .

Clearly, due to the random spatial variation of the refractive index, the wave experiences distortion and aberration. The magnitude of the wave front aberration is related to the refractive index structure constant and the path length.

Particularly, the phase aberration manifests itself when an imaging system is used. Consider a generic imaging system (e.g., a telescope) with an entrance pupil aperture of diameter  $D$  and focal length  $F$ . According to diffraction is theory, when a plane wave is projected on the focal plane, the spatial distribution of the intensity is described by the Airy pattern as

$$I(r) = I_o \left( \frac{2J_1\left(\frac{\pi Dr}{\lambda F}\right)}{\left(\frac{\pi Dr}{\lambda F}\right)} \right)^2 \quad (8.45)$$

where  $r$  is the distance from the center of the focal plane and  $I_o$  is the peak intensity at the center. The full-width-half-maximum of the Airy pattern is the diffraction-limited spot size at the focal plane ( $d_{dl}$ ) is

$$d_{dl} = \frac{\lambda}{D} F, \quad (8.46)$$

which indicates the larger is the aperture diameter  $D$  the better is the system resolution. The resolving power (or the resolution) of a diffraction telescope [20] can be defined as the integral

of the optical transfer function of the optical system, that for a diffraction limited system is

$$\mathcal{R}_{dl} = \frac{\pi}{4} \left( \frac{D}{\lambda F} \right)^2 \quad (\text{cycle/m})^2 \quad (8.47)$$

In the presence of clear air turbulence, the telescope resolving power will be degraded because of the wave front phase aberration will affect the system resolving power. In other words, one should expect that in the presence of clear air turbulence, the telescope resolution (and the minimum spot size at the focal plane) would be bounded not only by the telescope aperture, but also by the strength of the turbulence. Particularly in Ref. [20] is described how in the presence of clear air turbulence the telescope resolving power degrades, this degradation can be approximately expressed in closed form as [2]

$$\mathcal{R} = \frac{\pi}{4} \left\{ \frac{1}{\lambda F} \frac{D}{[1 + (D / r_o)^{5/3}]^{3/5}} \right\}^2 \quad (8.48)$$

as where the  $r_o$  is the Fried parameter or atmospheric coherence length (to be defined later) which is related to the strength of the optical turbulence. Equation 8.42 indicates that large aperture telescope resolution is lower bounded by the diffraction limited value when  $D \ll r_o$  (weak or no optical turbulence) and to a saturation value when  $D \gg r_o$  (strong turbulence)

$$\mathcal{R}_{\text{sat}} = \frac{\pi}{4} \left( \frac{r_o}{\lambda F} \right)^2 \quad (8.49)$$

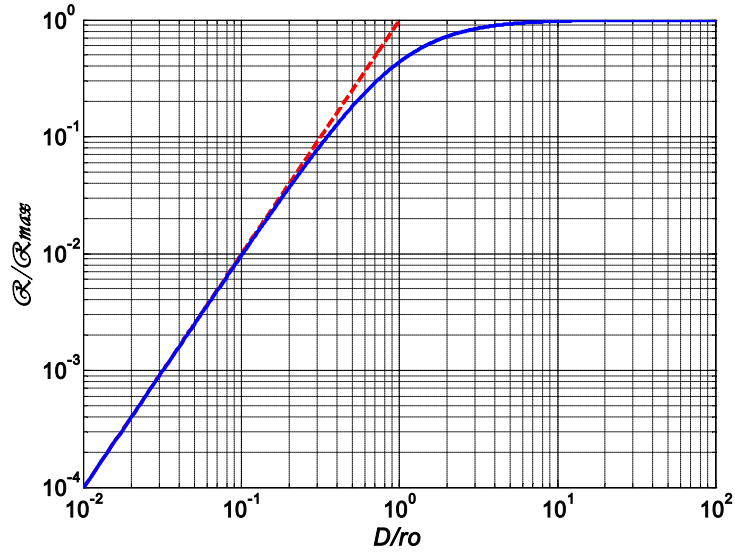


**FIGURE 8.5** Telescope resolution in the presence of clear air turbulence. As  $D/r_0 > 2-3$ , the telescope resolution already converge to  $\mathcal{R}_{\text{clear}}$ . At  $D/r_0 = 1$ , it corresponds the knee of curve.

Explanation of the physical meaning of the atmospheric coherence length can be visualized when the telescope resolution as  $\mathcal{R}/\mathcal{R}_{\text{clear}}$  plotted as function of the ratio  $D/r_0$ , as seen in Figure 8.5. At  $D/r_0 = 1$  corresponds the knee of the telescope resolution curve, after  $D/r_0 = 1$  the telescope resolution starts deviating from the diffraction limit of  $\mathcal{R}$ . In fact, for  $D/r_0 \sim 2-3$ , the telescope resolution rapidly converges to a resolution close to  $\mathcal{R}_{\text{clear}}$  as in Equation 8.49.

As already done for other figure of merits of the turbulence,  $r_0$  can be described as a function of the refractive index structure parameter, wavelength, and wave front. Particularly, in the case of a plane wave propagating from the altitude  $h_0 + L$  to  $h_0$  (downlink), one has [3]

$$r_0 = \left[ 0.423 \sec(\theta) k^2 \int_{h_0}^{h_0+L} C_n^2(h) dh \right]^{-3/5}, \quad (8.50)$$

where  $\theta$  is the angle from the zenith in the slant path; for the horizontal path of length  $L$  at constant  $C_n^2$

$$r_0 = (0.423k^2 C_n^2 L)^{-3/5}. \quad (8.51)$$

For a spherical wave instead we have (downlink)

$$r_0 = \left[ 0.423 \sec(\theta) k^2 \int_{h_0}^{h_0+L} C_n^2(h) \{(L + h_0 - h) / L\}^{5/3} dh \right]^{-3/5}, \quad (8.52)$$

while for a horizontal path

$$r_0 = (0.158k^2 C_n^2 L)^{-3/5}. \quad (8.53)$$

Notice that, with the help of the Fried parameter one can conveniently rewrite the phase structure function in Equation 8.44 as

$$D_\phi(\mathbf{R}) = 6.88 \left( \frac{\mathbf{R}}{r_0} \right)^{5/3}. \quad (8.51)$$

The atmospheric coherence length,  $r_0$ , is a crucial parameter describing the turbulence the quality of the wave front that is propagating in the atmosphere, particularly it follows that:

1.  $r_0$  is the diameter of an equivalent aperture where the phase variation in rms is

approximately 1 rad.

2.  $r_0$  is the diameter of an equivalent aperture where the telescope resolution is approximately the same (diffraction limited) in absence of turbulence: the larger  $r_0$  is the smaller the effects of turbulence on the propagating wave.
3.  $r_0$  varies with the wavelength as  $\lambda^{6/5}$ ; therefore, at larger wavelengths of operation the Fried parameter has larger values which imply a less severe turbulence effect on the wave front.
4.  $r_0$  values vary depending on location, time of the day; for example, for a given astronomical telescope location, nighttime (favorable) values at  $\lambda = 500$  nm can be 10 cm or above.
5. According to Equation 8.52, the turbulence in the proximity of the receiver (pupil plane) affects with larger weight the atmospheric coherence length. Hence, in a space-to-Earth satellite link one should expect large atmospheric coherence length at the satellite (uplink), and smaller  $r_0$  with more severe phase distortion at the ground station receiver (downlink) Figure 8.6.
6. The ratio between the wavelength of operation  $\lambda$  and the Fried parameter (at the wavelength of operation) defines the telescope (or receive system) angular resolution or more commonly named astronomical seeing as [21]

$$\text{seeing} = \frac{\lambda}{r_0} \cdot \text{rad} \quad (8.55)$$

The seeing is also related to the size of the full-width-half-maximum or spot size of the intensity pattern at the focal plane. In fact, for a receiving optical system with focal length  $F$  and aperture diameter  $D \gg r_0$ , the related spot size at the focal plane will be

$$d_{\text{seeing}} = \frac{\lambda}{r_0} F, \quad (8.56)$$

with  $d_{\text{seeing}} \gg d_{\text{dl}}$ .

Equation 8.56 implies that, for large seeing (small  $r_0$  and strong turbulence) values, the received signal spot size at the focal plane can be relatively large, with the consequence that all signal photons can be captured only using a larger surface area photodetector. Conversely, the use of a large surface photodetector can limit the receiver electrical bandwidth and, consequently, the detection of the digital signal at high bit rate. At the same time, if a single detector is used with a diameter smaller than  $d_{\text{seeing}}$ , the receiver will experience an additional loss of signal that for a number of applications (e.g., deep-space optical communications) cannot be sustainable.

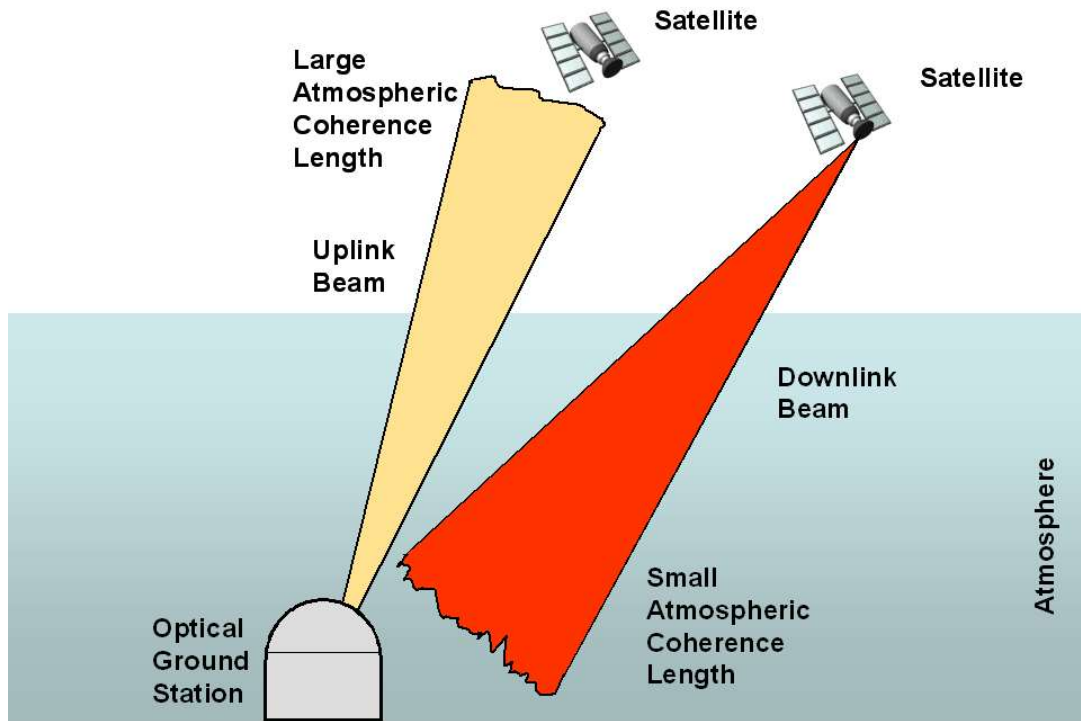


**FIGURE 8.6** Atmospheric coherence length is affected in different fashions for uplink and downlink. For downlink,  $r_0$  is much smaller with respect to what one experienced at

**the satellite during uplink.**

However, analysis of the aberrations of the wave front phase with the help of adaptive optics can help limit the consequences of signal spot blurring at the focal plane. The blurring of the spot at the receiver focal plane (as indicated in Equation 8.56) refers to a long exposure when all the distortion components are integrated in time. Instead, when observing the time evolution of the signal spot at the focal plane, one would notice that the spot itself is moving (or dancing) randomly around a central position (centroid motion). This first-order effect is due to the random fluctuations of the angle of arrival of the signal wave front induced by the turbulence. The angle of arrival perturbation has a Gaussian distribution described by a zero mean and variance along the  $x$  and  $y$  axes as [22]

$$\sigma_{\alpha x}^2 = \sigma_{\alpha y}^2 = 0.182 \left( \frac{D}{r_0} \right)^{5/3} \left( \frac{\lambda}{D} \right)^2. \quad (8.57)$$

Recalling that  $r_0$  varies with the wavelength as  $\lambda^{6/5}$ , and noting Equation 8.57, it is simple to derive that the spot centroid motion at the focal plane is independent of the wavelength, while it represents a larger component of the spot blurring at longer wavelengths. With the help of Equations 8.42 and 8.51, Figure 8.7 plots the ratio between the angle arrival error (standard deviation) and the angular resolution of a telescope in function of  $D/r_0$ . Figure 8.7 illustrates that for  $D/r_0 \sim 3$ , the angle of arrival fluctuation is the more sizeable component of the enlargement of the spot size at focal plane and its removal can benefit the receiver operation. For larger  $D/r_0$  values, instead, higher order wave front distortion (astigmatism, coma, etc.) contributes more heavily in the blurring of the signal spot.

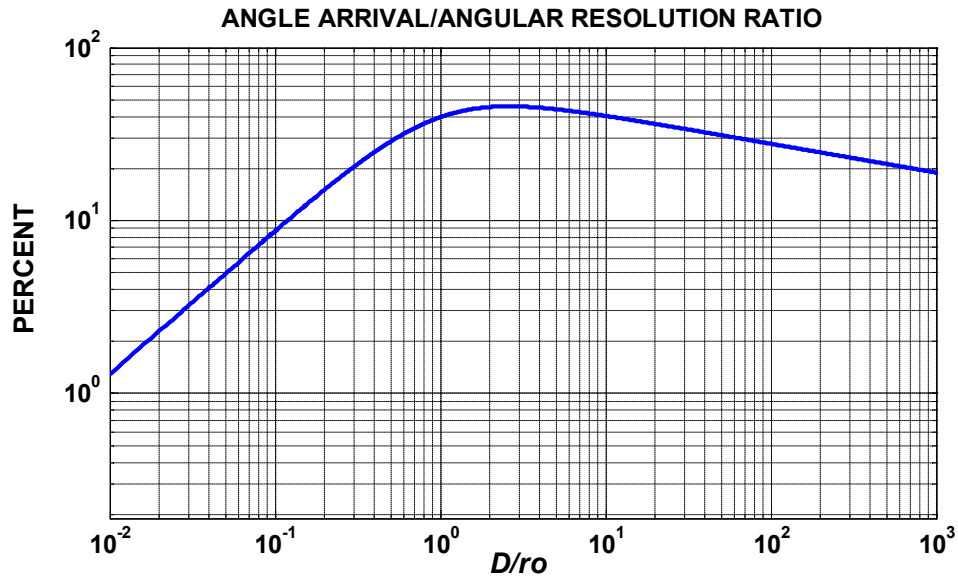


**FIGURE 8.7** Ratio between the angle of arrival standard deviation and angular resolution of a telescope. The ratio peaks for  $D/r_0 \sim 3$ .

Adaptive optics techniques can be used to reduce the size of the distorted spot size at the focal plane and to reduce it to a size closer to its diffraction limit [22].

Removal of the fluctuations of the angle of arrival was historically the first adaptive optics technique ever attempted [23], and it is conceptually illustrated in Figure 8.8. In essence, in Figure 8.8, a beam splitter removes a part of the incoming signal and redirects it to a wave front sensor that is able to (a) determine the instantaneous angle of arrival, and then (b) address a correction to a tip-tilt mirror that compensates the angle arrival offset and stabilizes the incoming beam.



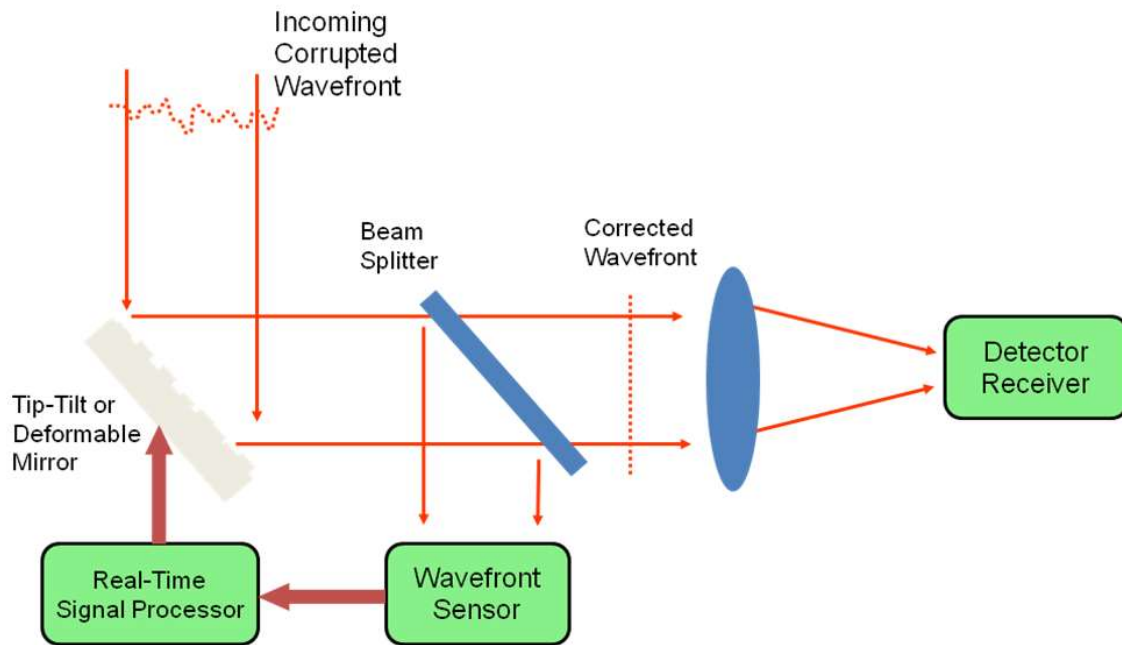


**FIGURE 8.8** Block diagram for a generic adaptive optics system. The mirror on the path can represent either a tip-tilt system for angle of arrival compensation or a deformable mirror for higher order phase compensation.

The simplest form of this wave front sensor can be constituted by a quadrant detector (consisting of four element pixels) or a CCD camera, both sensors able to determine the position of the centroids of the focused signal [22]. The acquired information of the centroid location on a focal plane can then be converted as tip-tilt angular information that drives the correction of the input tip-tilt mirror.

Adaptive optics compensation of higher order distortions of the beam wave front is possible [22]. Under this scenario, a more complicated action of the correcting mirror is required (besides tip-tilt). Mainly, a spatially deformable mirror driven by the signal of the wave front sensor of Figure 8.8 is needed for this scope. In this configuration, the spatially deformable mirror needs to be able to compensate for local aberration of the wave front [22, 24]. Temporal

response of the correction of the actuator elements via the input deformable mirror is related to the turbulence time constant. The Greenwood frequency [25] is used to describe how fast the adaptive optics system needs to respond to the variation of the atmospheric turbulence. Related to turbulence strength and the transversal component of the wind speed  $[v(h)_T]$  along the line of sight receiver–transmitter, the Greenwood frequency is given by

$$f_G = \left[ 0.102 k^2 \sec(\theta) \int_{h_0}^{L+h_0} C_n^2(h) v_T(h)^{5/3} dh \right]^{3/5} \text{ Hz}, \quad (8.58)$$

where  $f_G$  can vary from tens to hundreds of hertz depending on the wind speed and turbulence strength. Generally, an adaptive optics system is required to have a close loop frequency atleast four times  $f_G$ .

Conversely, in a number of applications, the signal level of the received beam can be too low for driving an adaptive optics system. In this case, sources other than the incoming signal can be used for the correction of the deformable mirrors. For instance, in astronomical telescopes, such external sources can be a star or a backscattering signal from a laser beacon [22, 24]. It is essential, however, that the spatial description of the atmospheric turbulence carried by an external source represents that experienced by the incoming signal. To do so, the angular separation between the signal beam and the external source must be less than the isoplanatic angle [26] given by

$$\vartheta = \left[ 2.91 k^2 \sec(\theta)^{8/3} \int_{h_0}^{L+h_0} C_n^2(h) h^{5/3} dh \right]^{-3/5} \text{ rad.} \quad (8.59)$$

Typical values of the isoplanatic angle seen by a ground telescope can vary from a few to tens

of microradians.

### 8.1.9 BEAM EFFECTS

To complete our discussion of the effects of clear air turbulence on laser beam propagation in the atmosphere, the so-called beam effects need to be addressed. Generally, when a beam is propagating in the atmosphere, additional consequences of the action of clear air turbulence (besides scintillation and phase degradation of the wave front) are beam spreading and beam wander.

Beam spreading describes the broadening of the beam size at a target beyond the expected limit due to diffraction (or optical elements in the beam path), as the beam propagates in the turbulent atmosphere. Another effect of the turbulence on the beam propagation is relatively slow wandering of the beam around its central axis in a random fashion. A result of beam spreading and beam wander is that the long term averaged beam irradiance at a given point is below an expected value, and manifests itself as a loss of signal. Beam spreading and beam wander particularly affect the propagation of uplink (ground-to-space) and horizontal atmospheric path link. To describe these effects for a Gaussian beam we recall that given a collimated propagating Gaussian beam at a distance  $\mathbf{z}$  from the source, the irradiance along a plane normal to the propagation direction is

$$I(\mathbf{z}, r) = \frac{2P_0}{\pi\omega^2(\mathbf{z})} \exp\left(-\frac{2r^2}{\omega(\mathbf{z})^2}\right) (\text{W/m}^2), \quad (8.60)$$

where

$P_0$  is total (source) beam power in Watts

$r$  is the radial distance from the beam center

$\omega(\mathbf{z})$  is the (radial) beam waist that after a propagation distance  $\mathbf{z}$  (or in the case of an uplink beam is the slant path from ground to space) is given by

$$\omega(\mathbf{z})^2 = \omega_0^2 \left[ 1 + \left( \frac{\mathbf{z}}{Z_0} \right)^2 \right] (\text{m}^2), \quad (8.61)$$

in which  $\omega_0$  is the initial beam waist at  $\mathbf{z} = 0$  and  $Z_0$  is the Rayleigh distance given by

$$Z_0 = \frac{\pi \omega_0^2}{\lambda} (\text{m}). \quad (8.62)$$

Beside the Rayleigh distance, the concept of the full divergence angle,  $\theta_{DIV}$ , as the angle that comprise the 86.5% of the beam energy is defined as

$$\theta_{DIV} = \frac{2\omega(\mathbf{z})}{\mathbf{z}} = \frac{2\lambda}{\pi \omega_0} \quad (8.63)$$

Again, Equation 8.54 refers to a generic Gaussian beam propagating in free space in the absence of optical turbulence. Conversely, when optical turbulence is present, the beam will experience a degradation in beam quality with a consequence that the long term averaged beam waist in time will be  $\omega_{eff}(\mathbf{z}) > \omega(\mathbf{z})$ . Then one can write the irradiance of the beam averaged in time as

$$I(\mathbf{z}, r) = \frac{2P_0}{\pi\omega_{\text{eff}}^2(\mathbf{z})} \exp\left(-\frac{2r^2}{\omega_{\text{eff}}^2(\mathbf{z})}\right). \quad (8.64)$$

The effective waist,  $\omega_{\text{eff}}(\mathbf{z})$ , describes the variation of the beam irradiance averaged over long term at a distance  $\mathbf{z}$  from the source. However, over short term, one notices that the beam will not only experience a spreading beyond what is expected in the absence of turbulence, but the beam spot itself will wander around a center position. This beam wandering, among other things, can be an additional cause of fluctuation (in addition to scintillation) of the signal irradiance at the targeted receiver. If we indicate as  $r_c$  the distance of the beam centroid from the center one can express the effective beam waist as [27].

$$\omega_{\text{eff}}^2(z) = \omega_{\text{st}}^2(z) + \langle r_c^2 \rangle \quad (8.65)$$

where  $\omega_{\text{st}}(\mathbf{z})$  is the beam waist portion affected by (short term) beam spreading and  $\langle r_c^2 \rangle$  is variance of the beam wander radial displacement that for an uplink beam is [27]

$$\langle r_c^2 \rangle = 0.54z^2 \left(\frac{\lambda}{2\omega_o}\right)^2 \left(\frac{2\omega_o}{r_o}\right)^{5/3} \quad (8.66)$$

in which  $r_o$  is atmospheric coherence length as Eq. (8.50).

Evidently, due to the fact that  $\omega_{\text{eff}}(\mathbf{z}) > \omega(\mathbf{z})$ , the beam will experience an average reduction of the irradiance at the beam center (on axis) [27]

$$\langle S \rangle = \frac{\omega(z)^2}{\omega_{\text{eff}}^2(z)} = \frac{1}{[1 + 5.65(\omega_o / r_o)^{5/3}]^{6/5}} \quad (8.67)$$

Equation (8.67) defines the term  $\langle S \rangle$  named as atmospheric Strehl ratio for the conditions from weak to strong turbulence. Conversely, the atmospheric Strehl ratio can be considered as another source of signal loss (with respect to the ideal propagation as in Eq. (8.60)), and therefore must be taken into consideration when budgeting the signal power (e.g. optical link budget). In a number of applications, bidirectional ground-to-space links (uplink and downlink) can be established, in this case a control loop can track the downlink beam, to correct the uplink tilt caused by the optical turbulence and remove the beam wander degradation for the uplink beam. In this case it is shown [27] that the corrected atmospheric Strehl ratio,  $\langle S_{tr} \rangle$ , can be expressed as

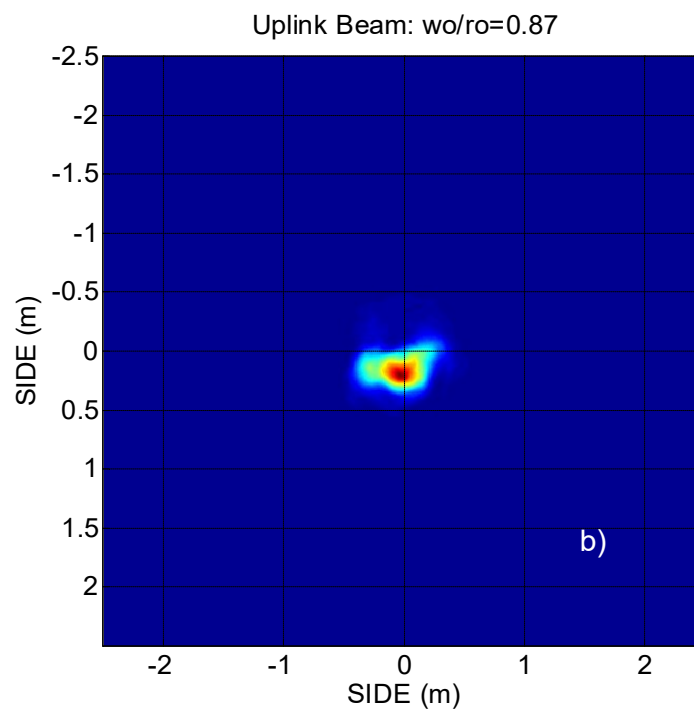
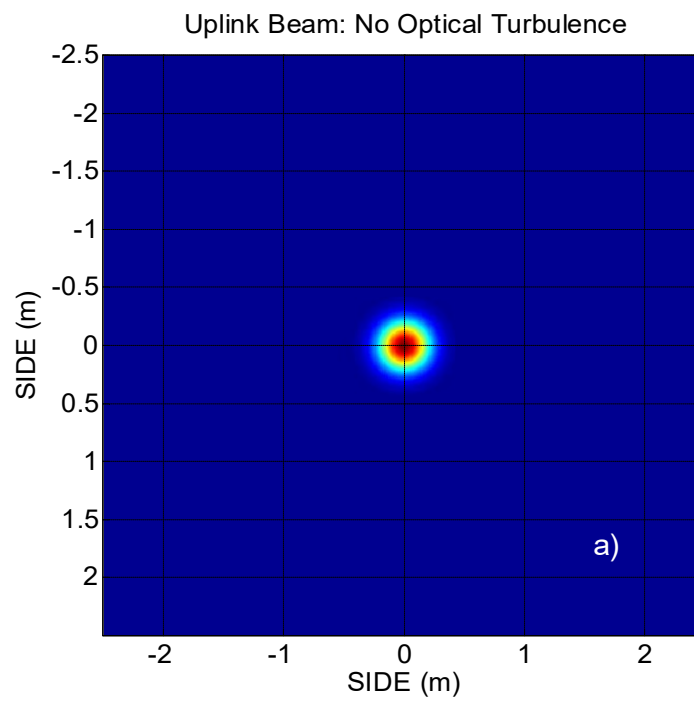
$$\langle S_{tr} \rangle \cong \frac{1}{[1 + \left( 5.65 - \frac{4.86}{1 + 0.04(\omega_o/r_o)^{5/3}} (\omega_o/r_o)^{5/3} \right)^{6/5}}]^{6/5}} \quad (8.68)$$

The atmospheric Strehl ratio is a good description of how the propagation of a Gaussian beam is affected by the optical turbulence averaged over long term. Generally, to understand the possible effects of the optical turbulence on Gaussian beam the ratio between the beam waist at the source,  $\omega_o$ , over the atmospheric coherence length as seen by the source on the ground, Eq. 8.50, is a good metric. Essentially, one may consider three condition of operations: a)  $\omega_o/r_o \ll 1$ , weak turbulence, where the beam is less affected by the optical turbulence, and the beam at target is not distorted by the turbulence; b)  $\omega_o/r_o \sim 1$  where beam is mainly affected by radial displacement that leads to beam wander in time around the optical axis; c)  $\omega_o/r_o \gg 1$ , strong turbulence, where the beam wander is more detectable in addition to the fact the short term realization of the beam at the target may break up showing a number of hot spots or ‘speckles’. To better illustrate this concept, Fig. 8.9 depicts realizations of beam propagation

under three different condition of turbulence. The figure refers to the case of a propagation of a Gaussian beam at a wavelength of 1064 nm with a beam waist  $\omega_0 = 7\text{cm}$ . The beam is propagating in the atmosphere with at zenith angle of  $60^\circ$  with instantaneous images of the beam after a path of 60 Km from the source. The images are produced using a wave-optics code and a Hufnagel-Valley profile of the turbulence at different turbulence strength as in Fig. 8.9b) and 8.9 c). Notice, that the figures represent just a single realization of the effect of the turbulence for a short exposure, while Strehl ratio of Eq. 8.67 (and 8.68) refers to a long term average of the beam shape affected by the turbulence. Particularly, Figure 8.9-a) depicts the beam at 60Km of distance from the source in (hypothetical) absence of turbulence, the beam is centered around the central axis and the beam size is as indicated in Eq. 8.64. Instead, Fig. 8.9-b) describes a realization for  $\omega_0/r_0 = 0.87$ , with  $r_0 = 8.19\text{ cm}$  at 1064 nm along the line of sight. The beam shape is still generally Gaussian experiencing some distortions, however, due to the turbulence the beam is moving around the central axis, in fact for this specific image the centroid coordinates are off center of 12 cm and 4 cm in the  $x$  and  $y$  directions. The beam will continue to wander around the central axis, and the final integrated long term beam waist,  $\omega_{\text{eff}}(\mathbf{z})$ , can be calculated using Eq. 8.67.

Finally, in Figure 8.9-c) is the depicted a realization for  $\omega_0/r_0 = 2.75$ , with  $r_0 = 2.55\text{ cm}$  at 1064 nm along the line of sight. In this case the beam experiences a strong degradation losing its spot-like shape and breaks up in ‘speckles’. In Fig. 8.9-c) the coordinates of the beam centroid are -59 cm and -16 cm respectively along the  $x$  and  $y$  axis. Of course, in time the beam continues to wander around the central axis, breaking up in different shapes, while the long term average shape of the beam is described by Eq. 8.67. Finally, Fig. 8.9-d) is comparing the long term average distribution of the beam intensity for the three cases here described according to Eq. 8.67. The atmospheric Strehl ratio greatly changes for the case for the case  $\omega_0/r_0 = 0.87$ , and  $\omega_0/r_0 = 2.75$ , with loss 8.7 and 18 dB respectively when compared to the ideal case of Fig.

8.9-a).





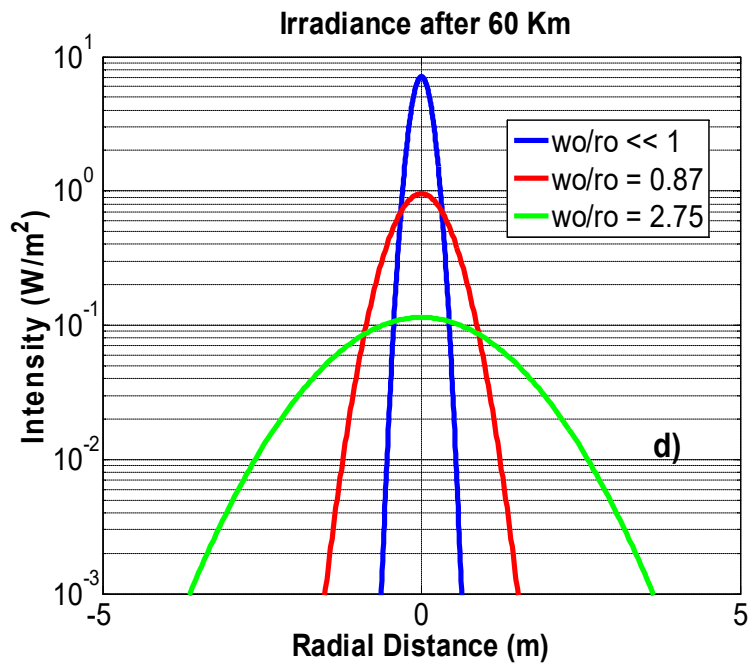
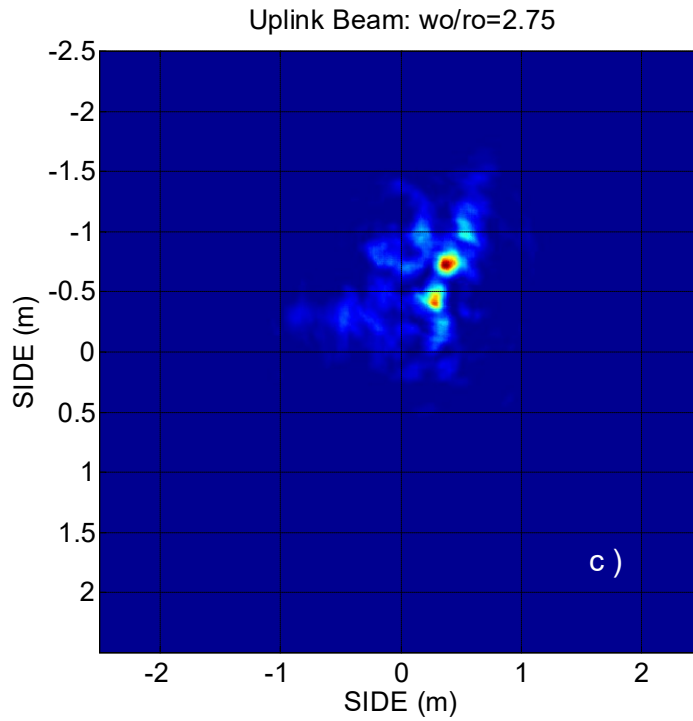


**FIGURE 8.9** Three different realizations of a Gaussian beam spot for 60 km path in the atmosphere with a zenith angle of  $\theta=60^\circ$ . The initial beam waist is of 7cm, while the

wavelength is 1.064  $\mu\text{m}$ : (a) absence of turbulence; (b) weak turbulence with  $r_o=8.19\text{cm}$  (c) strong turbulence with  $r_o=2.55\text{cm}$ ; d) long term averaged radial distribution of beam intensity after 60 Km.

## 8.2 ATMOSPHERIC TRANSMISSION LOSS AND SKY BACKGROUND NOISE

### 8.2.1 ABSORPTION AND SCATTERING

Earth's atmosphere, via absorption and scattering, attenuates a propagating electromagnetic wave. Considering a collimated beam of initial beam intensity  $I(0)$ , after a path of length  $L$ , the atmospheric transmittance  $T_{\text{atm}}$  related to atmospheric attenuation may be described by Beer's law as

$$I(L) / I(0) = T_{\text{atm}} = \exp\left(-\int_0^L \alpha(z) dz\right) = \exp(-\tau), \quad (8.69)$$

where

$\tau$  is the optical depth of the path

$\alpha$  (dimensionally  $\text{km}^{-1}$  or  $\text{m}^{-1}$ ) is the extinction or attenuation coefficient

In case of constant attenuation coefficient (e.g., horizontal path in the atmosphere) one finds

$$\tau = \alpha L. \quad (8.70)$$

The optical depth is related to the atmospheric loss,  $L_{\text{ATM}}$  that can be expressed in dB as

$$L_{\text{ATM}} = -10 \log_{10} T_{\text{atm}} = 4.34 \tau \text{ (dB)}. \quad (8.71)$$

The extinction coefficient is greatly dependent on the wavelength of operation, and can be considered the sum of the absorption coefficient  $\alpha_A$  and scattering coefficient  $\alpha_S$ . At the same time, both  $\alpha_A$  and  $\alpha_S$  have a contribution from the molecular and aerosol constituents of the atmosphere. In summary, one can write

$$\alpha = (\alpha_{\text{AM}} + \alpha_{\text{AA}}) + (\alpha_{\text{SM}} + \alpha_{\text{SA}}). \quad (8.72)$$

Molecular absorption of the gases manifests itself with narrow absorption lines due to the resonance of photon energy, with molecules (and atoms) of the gas and water vapor present in the atmosphere. Of course, due to the variable density of the atmosphere constituents with altitude, the molecular absorption will be of different strengths at different elevations above sea level.

Molecular scattering, otherwise indicated as Rayleigh scattering, has a spectral dependence as [28]

$$\alpha_{\text{SM}} = C_R / \lambda^4, \quad (8.73)$$

in which,  $C_R$  is a term depending on the different particle cross sections and concentrations, while the wavelength dependence indicates that Rayleigh scattering is stronger at shorter wavelengths (i.e., visible wavelengths), and it is less important at wavelengths in the near-infrared or longer.

Conveniently, for a ground-to-space link, one can approximate the optical depth (ground-to-

space) due to Reyleigh scattering only in a first order as [29]:

$$\tau_{SM}(\lambda) = \frac{p}{p_o} 0.00877 \lambda^{-4.05} \quad (8.74)$$

where  $p$  is the atmospheric pressure at location of interest,  $p_o$  is the atmospheric pressure at sea level, and the wavelength of interest  $\lambda$  is in microns.

Aerosols are particles suspended in the atmosphere with different concentrations. They have diverse nature, shape, and size. Aerosols can vary in distribution, constituents, and concentration. As a result, the interaction between aerosols and light can have a large dynamic, in terms of wavelength range of interest and magnitude of the atmospheric scattering itself. Because most of the aerosols are created at the earth's surface (e.g., desert dust particles, human-made industrial particulates, maritime droplets, etc.), the larger concentration of aerosols is in the boundary layer (a layer up to 2 km above the earth's surface). Above the boundary layer, aerosol concentration rapidly decreases. At higher elevations, due to atmospheric activities and the mixing action of winds, aerosol concentration becomes spatially uniform and more independent of the geographical location.

Scattering is the main interaction between aerosols and a propagating beam. Because the sizes of the aerosol particles are comparable to the wavelength of interest in optical communications, Mie scattering theory is normally used to describe aerosol scattering [30, 31]. Such a theory specifies that the scattering coefficient of aerosols is a function of the aerosols their size distribution, cross section, density, and wavelength of operation.

For horizontal link, one can use a semi empirical method to describe and scale the scattering extinction coefficient. In a horizontal path, when the aerosol scattering is constant, it is defined the visual range  $V$ , for a wavelength of  $\lambda = 550$  nm, as the distance in (Km) where the total atmospheric loss is approximately 17 dB, or  $\alpha V = 3.91$ . Founding  $V$ , one can approximate the aerosol scattering extinction coefficient as [30]

$$\alpha_{SA} = (3.91/V)(550/\lambda_c)^\delta \quad (8.75)$$

in which the wavelength of operation  $\lambda_c$  is expressed in nm, and the visual range is  $V$  indicated in km. The exponent  $\delta$  is (approximately) related to  $V$  as

$$\delta = 0.585V^{1/3} \quad (8.76)$$

The value of  $V$  for a typical clear day can be  $V = 23$  km (corresponding to a  $\delta = 1.6$ ) or better, while for a hazy day the visual range may have a value of  $V = 5$  km ( $\delta = 1$ ). The values the exponential number assumes in Equations 8.73 and 8.74, (i.e.,  $\delta \ll 4$ ) indicates that aerosol scattering can substantially contribute to the overall extinction of the optical beam in the visible as well as in the near-infrared when compared to Rayleigh scattering.

The mechanism of absorption and scattering have been understood and characterized with a large degree of accuracy, and therefore a number of atmospheric radiative transfer software simulation packages have been developed to describe the effects of atmospheric absorption and scattering under different atmospheric conditions and over a large wavelength range. Historically, one of the first software programs describing the atmospheric effects on a laser beam was LOWTRAN (acronym for **LOW** resolution atmosphere **TRAN**smission) [32] developed by the U.S. Air Force. LOWTRAN can be used to describe atmospheric transmittance and radiance in the wavelength range 0.2–28.5  $\mu\text{m}$  (i.e., 350–40,000  $\text{cm}^{-1}$ ) with a resolution of 20  $\text{cm}^{-1}$ . During a simulation, the software divides the atmosphere between sea level and 100 km altitude (or less) up to 33 layers. Each atmospheric layer is described by a variation of temperature, pressure, gas composition, gas mixing ratio, and aerosol distribution. The overall path atmospheric transmission (or optical depth) is calculated by compounding all

the possible layer contribution components along the path through the different atmospheric layers.

Concerning aerosol concentration, LOWTRAN provides a number of models apt to properly describe the nature of the aerosols (e.g., rural, urban, maritime, desert, etc.) and their distribution within the atmospheric profile (i.e., boundary layer, troposphere, stratosphere, etc.). Other meteorological conditions affecting the beam propagation (such as fog, clouds, cirrus clouds, and rain) can also be simulated. As an improvement to LOWTRAN, the simulation program MODTRAN (acronym for **MOD**erate atmospheric **TRAN**smission) [33] was developed, allowing a narrower spectral resolution up to  $0.2 \text{ cm}^{-1}$  in its more recent version MODTRAN 6 [34]. However, the requirement to properly model the propagation of laser beam with a narrow linewidth in the sub-angstrom range has inspired the development of software programs such as FASCODE (acronym for **FA**st atmospheric **S**ignature **CO**DE) [35] which can compute the atmospheric transmittance with line-by-line resolution. Concerning the remainder of this section, we will present a number of simulation results of atmospheric transmittance (and sky radiance) obtained using MODTRAN software program.

As an illustration of the effects of atmospheric interaction with an optical beam, Figure 8.10 depicts the case of atmospheric transmittance over a horizontal path of 10 km at sea level. The wavelength range is between 400 and 2500 nm, the visual range is 23 km (clear sky). In this simulation, the rural model is used for the aerosol distribution. The rural model is generally applied to describe locations (distant from urban centers and industrial areas) where aerosol particles are generated by vegetation, dust, etc. Specifically, the rural model assumes that the aerosol particles suspended in the atmosphere mainly consist of organic material mixed with water droplets.

Analyzing the transmittance spectrum, one can clearly notice that the spectrum itself is modulated between transmission bands with high transmittance and bands where the

transmittance is close to zero (forbidden bands). One of the main contributors to this modulation of atmospheric spectrum is water vapor, as seen in Figure 8.11, where the effects of water vapor are shown along with Rayleigh scattering and Mie scattering (each plotted distinctively). In the example represented in Figure 8.11, other molecular components actively contribute to modulate the transmittance spectrum, such as CO<sub>2</sub>, oxygen, etc. Usually, these gas elements' transition lines are very narrow with linewidth well below 1 Å. The effects of molecular and aerosol scattering to the transmittance spectrum appear more like a continuum, with molecular scattering disappearing at wavelength greater than 1 μm.

Interestingly, while the aerosol concentration is not very high in comparison to the other atmospheric constituents, aerosol scattering still has a sizeable effect over the transmittance spectrum, resulting one of the main limiting factor in the high transmittance bands in the infrared.

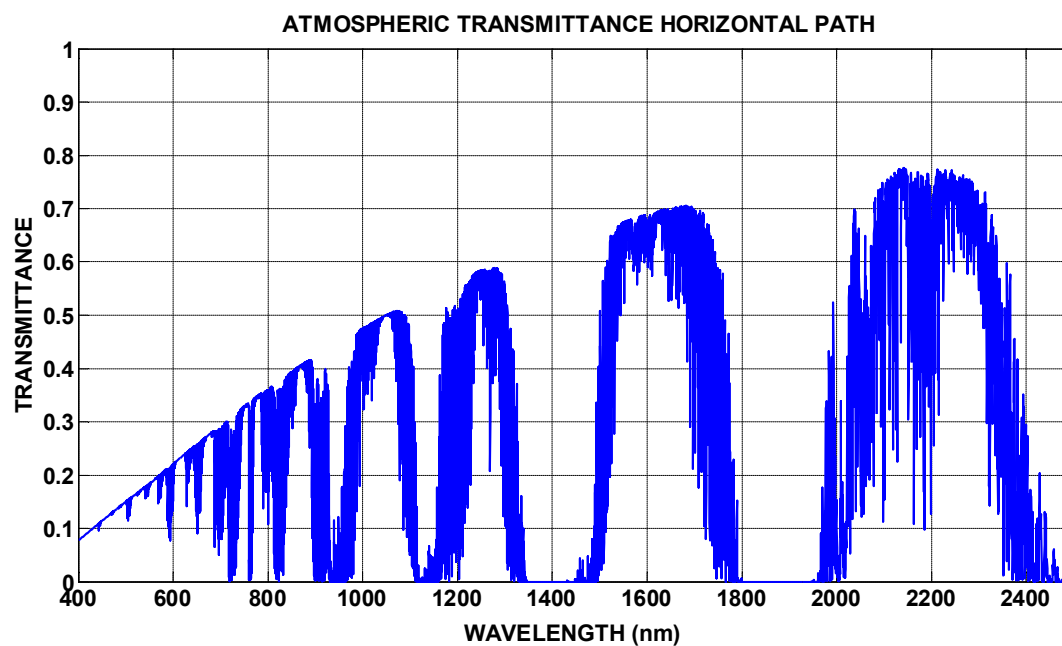


**FIGURE 8.10** Atmospheric transmittance over 10 km at sea level after a MODTRAN simulation. A model of rural aerosol with visual range of 23 km, corresponding to relatively clear sky, is assumed.



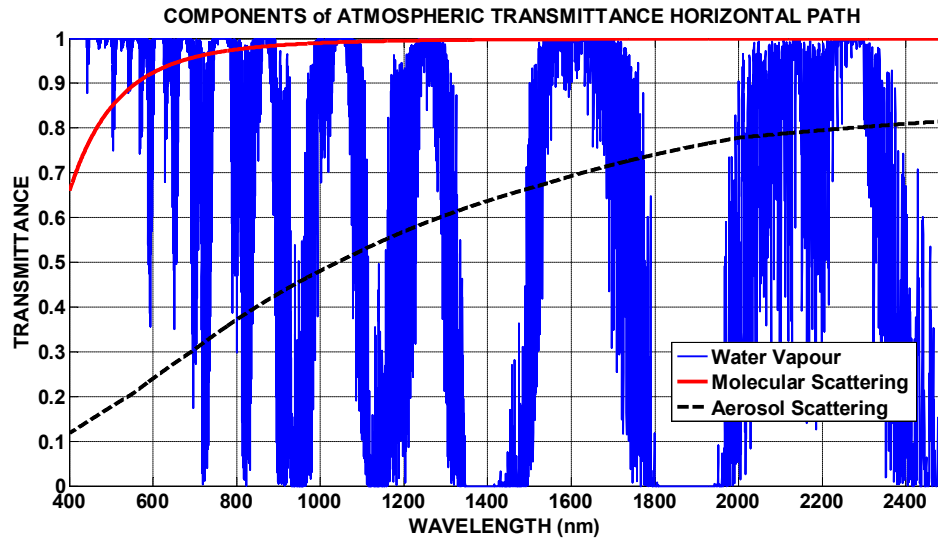


**FIGURE 8.11** Contribution of Rayleigh scattering, Mie scattering, and water vapor to the atmospheric transmittance as in Figure 8.1. Notice that the band structure is mainly due to water vapor. Effects of molecular scattering are not noticeable over 1000 nm, while aerosol scattering is noticeable all over the spectrum.

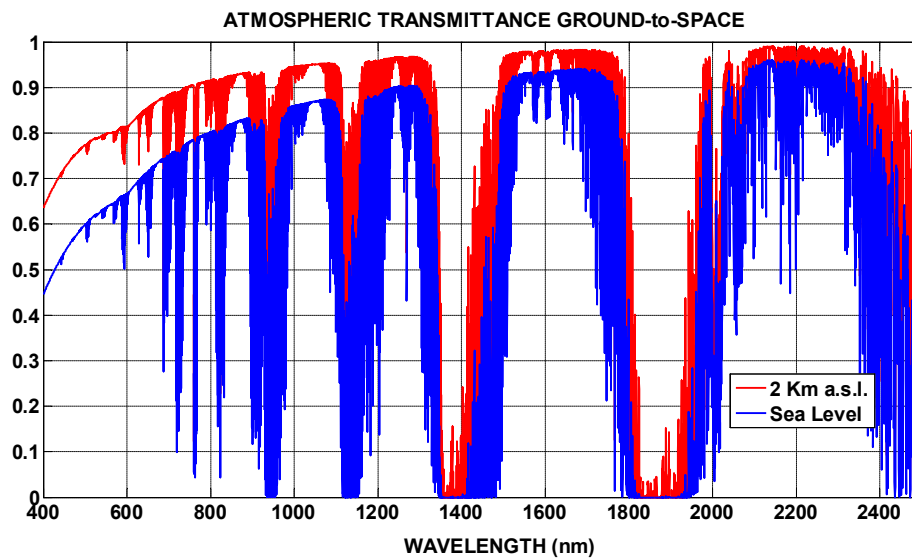


**FIGURE 8.12** Atmospheric transmittance in an Earth-to-space path at zenith. A rural aerosol composition with a surface visual range of 23 km is considered. The data refers to the case of an observer located at two elevations: sea level (lower

**transmittance) and 2 km above sea level.**

To complete the discussion on the atmospheric transmittance, Figure 8.12 illustrates the transmittance spectrum for a slant path, Earth-to-space. In this example, two ground levels considered, 0 (sea level) and 2 km (e.g., a mountaintop). Again, the wavelength range considered is 400–2500 nm with clear sky conditions and a visual range  $V = 23$  km. Even if a ground-to-space path is in order of tens of kilometers, the related transmittance is higher when compared to the same distance horizontal link. The reason for this difference is the diminishing atmospheric density at higher elevation, which causes an overall smaller interaction with the propagating light beam. Moreover, on a mountain top, aerosol concentration is greatly reduced, and so, one should expect for aerosol extinction.

To confirm this statement, Figure 8.13 shows and compares the contribution to the transmittance of aerosol scattering at an observation altitude of 0 and 2 km. It must be noticed that the plot of Figure 8.12 refers to the shortest (vertical) ground-to-space path at the zenith. In the case of a slanted path, Earth-to-space (or vice versa) with an angle  $\theta$  from the zenith, the path will be longer and the related atmospheric loss larger. However, if the optical depth at the zenith  $\tau(\lambda)$  is known, one can compute the atmospheric loss in dB at the zenith angle  $\theta$  as

$$L_{ATM}(\theta) = -10 \log_{10} T_{ATM}(\theta) = 4.34 \tau(\lambda) m(\theta) \quad (8.77)$$

where  $m(\theta) \geq 1$  is the relative air mass that takes into account the different contribution of a path length respect to zenith, corresponding to  $m(\theta = 0) = 1$ . Under the parallel plane approximation of the atmosphere (ignoring Earth's curvature), one can express the airmass as

$$m(\theta) = \sec(\theta) \quad (8.78)$$

with this expression valid up to  $\theta = 60^\circ$ . At larger zenith angle,  $60^\circ < \theta < 90^\circ$ , there a number

approximations can be for the relative airmass, including that one in Ref [36],

$$m(\theta) = \frac{1}{\cos(\theta) + 0.505572(96.07995 - \theta)^{-1.664}} \quad (8.79)$$

in which the angle  $\theta$  is expressed in degree.

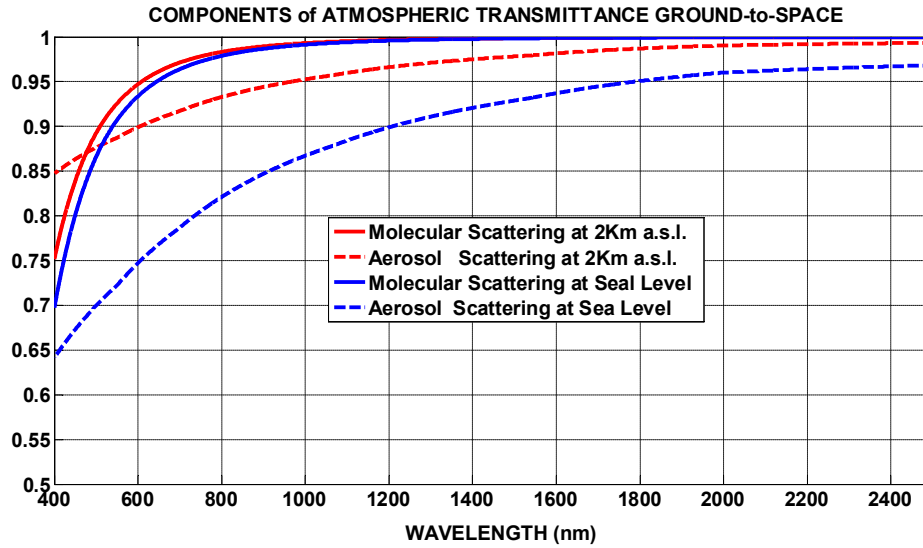


**FIGURE 8.13** Atmospheric transmittance in an Earth-to-space path at zenith. The observer is at two different altitudes (sea level and 2 km above sea level): (a) molecular scattering contribution at 2 km; (b) molecular scattering contribution at sea level; (c) aerosol scattering contribution at 2 km above sea level; and (d) aerosol scattering contribution at sea level. Data obtained after MODTRAN simulation.

### 8.2.2 BACKGROUND RADIATION AND SKY RADIANCE

In a number of applications, the receiver encompasses a source whose angular extension is larger than the receiver field of view. In this case, the extended source power captured by the optical receiver can be calculated when the source radiance  $B_\lambda$  is known, usually expressed

dimensionally in  $\text{W cm}^{-2} \text{sr}^{-1} \mu\text{m}^{-1}$ . The resulting optical power,  $P_R$ , captured in presence of an extended source is therefore

$$P_R = B_\lambda A_R \Omega_R \Delta\lambda L_T, \quad (8.80)$$

where

$A_R$  is the area of the receiver (or telescope) in  $\text{cm}^2$

$\Omega_R$  is the receiver field of view in solid angle

$\Delta\lambda$  is the system wavelength band of interest in  $\mu\text{m}$

$L_T$  is the optical system loss

In the case of space-to-ground optical communications, an extended source can be represented by planets, the Moon or (event not recommendable) the Sun. Those astronomical bodies can be (depending on the applications) either a signal source or source of background noise when they are in line of sight with the transmitter. In the latter case, the background radiance is received in addition to the optical signal and it negatively affects the receiver performances.

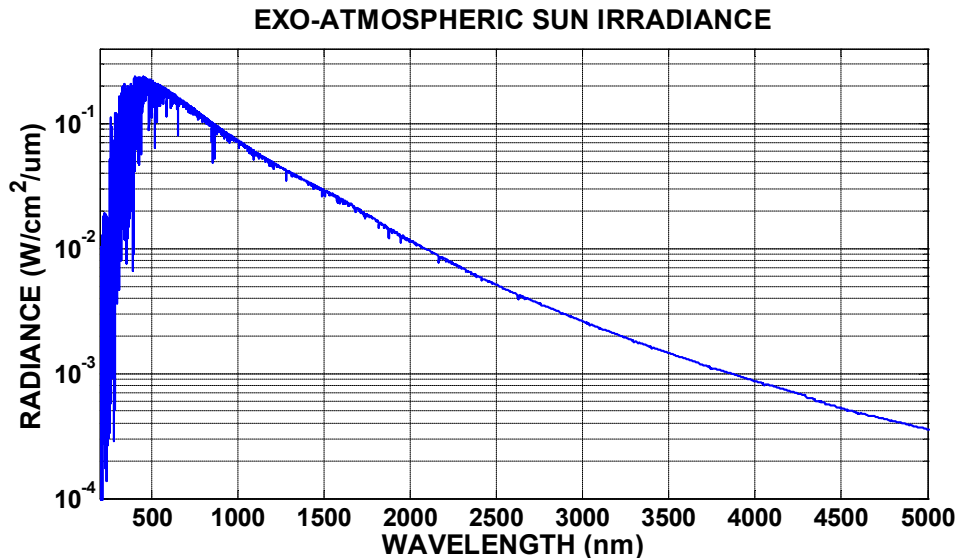


**FIGURE 8.14 Exo-atmospheric spectral irradiance of the Sun at a distance of 1 AU.**

Another common case where the background radiance constitutes a source of unwanted noise (for an optical communications receiver) occurs during daytime operations. Daytime sky radiance is originated by the scattering of the Sun irradiance. Spectrum of daytime sky radiance is correlated to Sun spectrum (Figure 8.14), which has its peak wavelength around 475 nm according to the properties of a blackbody emitter at a temperature  $T = 5800$  K.

As illustrated for the case of atmospheric transmittance, the diffused sunlight of the sky can be originated by molecular and aerosol scattering, with the latter being the prominent source of scattering (and sky radiance) in the near-infrared region. Because of the different concentrations of aerosols in the atmosphere, sky radiance is larger near ground and smaller at higher elevations. Moreover, sky radiance will depend on the angular proximity of the observer line of sight to the Sun, fast decreasing in a nonlinear fashion, as the angle separation from the Sun increases. As an example of the discussion, Figure 8.15 presents two cases of daytime spectral sky radiance. The Sun is at  $45^\circ$  from the zenith, the observer is at sea level looking up in the sky (as in the case of a downlink) at  $40^\circ$  and  $70^\circ$  from the zenith (Sun and downlink path are in the principal plane). The data are generated by a MODTRAN simulation, which uses a rural model to represent the aerosol concentration with a visual range of 23 km at the ground level. The figure clearly shows that for the direction closer to the Sun ( $5^\circ$ ), a receiver will experience the larger amount of sky radiance which will peak around 470 nm (peak of the Sun spectral irradiance).

The action of the atmospheric transmission manifests itself on the spectral radiance by modulating the values of radiance and causing forbidden bands (similar to the spectral transmittance of the atmosphere), where the sky radiance (and sunlight in general) is virtually zero. For wavelengths of  $1\text{ }\mu\text{m}$  and above, aerosol scattering is the main cause of sky radiance

and therefore one should expect that at locations with low aerosol concentration, this portion of the radiance spectrum will be smaller in magnitude. As a demonstration of this concept, Figure 8.16 shows sky radiance data, *ceteris paribus*, when the observer (or receiver during a downlink) is located at 2 km above sea level. At 2 km, the concentration of aerosol is lower than sea level with consequent lower sky radiance values with respect to those indicated in Figure 8.14.

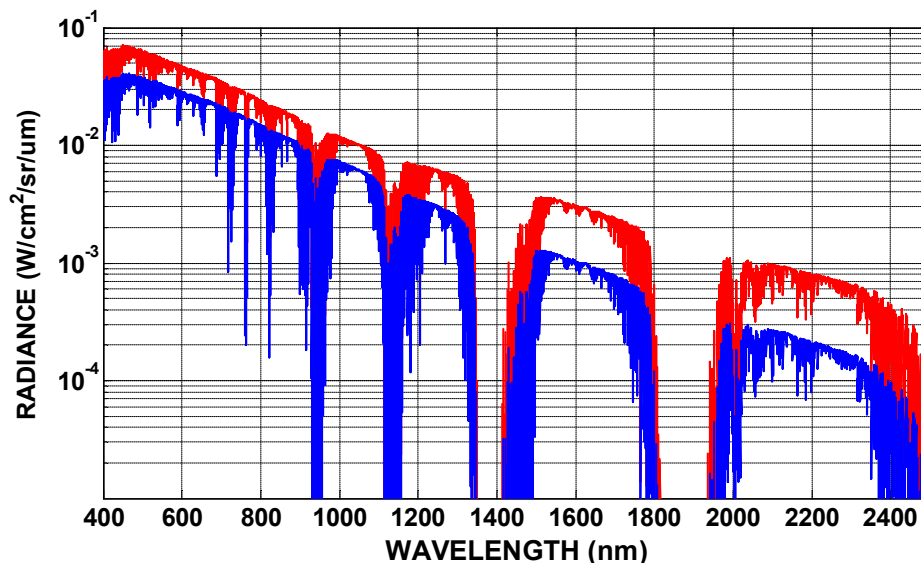


**FIGURE 8.15** Daytime sky radiance at sea level. The Sun zenith angle is 45°. Two cases (radiance curves) are shown: (1) the observer zenith angle on the ground is at 40° (higher radiance curve) and (2) the observer zenith angle on the ground is at 70° (lower radiance curve). The rural aerosol model with a visibility of 23 km at sea level was used. Data obtained after MODTRAN simulation.

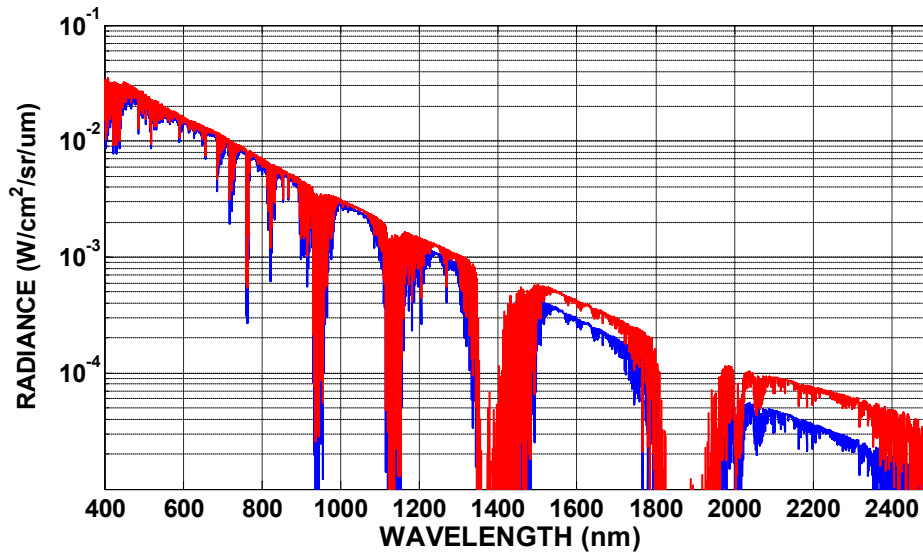


**FIGURE 8.16** Daytime sky radiance at 2 km above sea level. The Sun zenith angle is 45°. Two cases (radiance curves) are shown: (1) the observer zenith angle on the ground is at 40° (higher radiance curve) and (2) the observer zenith angle on the ground is at 70° (lower radiance curve). The rural aerosol model with a visibility of 23 km at sea level was used. Data obtained after MODTRAN simulation.

Clouds are another meteorological factor that contributes daytime sky radiance (besides the atmospheric opacity). Particularly noteworthy is the action of subvisual cirrus clouds that are composed of miniscule ice particles suspended high in the troposphere. These clouds affect the sky radiance in a mechanism similar to that of aerosols. MODTRAN and other similar software programs can also determine daytime sky radiance amount related to subvisual cirrus clouds. On the other hand, lower clouds have a more complex scattering mechanism including the fact that they can redirect sunlight irradiance in different directions in the sky, with the result that sky radiance is greatly dependent on the observation direction respect to the Sun and clouds position/distribution in the sky.

### 8.3 CONCLUSIONS

The purpose of this chapter is to help a system engineer consider the effects and consequences of the atmospheric channel in an optical link. The resulting system parameters (e.g., losses) could then be quantified and used in a link budget that hypothetically approaches design.

Concerning the effects of clear air turbulence of the atmospheric channel, it is observed that these are consequences of the random nature of the refractive index of air. Some of the key effects to consider are the fade (and surge) of the signal due to scintillations, additional losses due to beam spreading and beam wandering, and the focal plane losses experienced when a (larger) spot size is imaged on the detector. Expressions were provided for different link configurations (uplink, downlink, etc.) to allow an easy calculation of the relevant parameters that could be used in a possible control design table. However, it is worthy to repeat that all these effects (due to clear air turbulence) are related in magnitude on the strength of the turbulence itself as described by the profile of the structure parameter of the refractive index  $[C_n^2(h)]$ . Therefore, great care must be taken in the choice of  $C_n^2(h)$  that describes the turbulence. A number of parametric models of  $C_n^2(h)$  have been provided in this chapter, more are available in the literature. [2, 3]. Due to the random nature of the problem, it is quite difficult to properly represent all the possible variations of  $C_n^2(h)$  in time ( $C_n^2(h)$  changes can be very large during the 24 h of the day and during the year) and space (some locations can have more/less favorable  $C_n^2(h)$  profile). One way to partially solve (or bound) the problem is to assume a possible profile of  $C_n^2(h)$  (e.g., HV5/7) and then calculate the different parameters related to the clear air turbulence effects (e.g., beam spreading loss, probability of fade, etc.) while the profile is varied by a multiplicative factor (e.g.,  $0.5 \times \text{HV5/7}$ ,  $5 \times \text{HV5/7}$ , etc.). In this manner, one can predict how different turbulent strengths can affect the link. The



multiplicative factor can be determined either by some heuristic approach, or scaled by measuring some turbulence parameters such as the  $C_n^2$  close to the ground [37] or atmospheric coherence length [38].

Concerning atmospheric transmittance and sky radiance, these parameters can be obtained in principle by software simulation or by measurement in situ. However, after a number of measurement campaigns developed in recent years, one can also use the large number of data that already exists for the determination of atmospheric transmittance and sky radiance. For instance, the NASA AERONET program has deployed a number of sun-photometers around the world for the characterization of aerosol concentrations with measurements of the atmospheric transmittance and radiance. The AERONET Program [39], makes readily available a multi-year data bank of atmospheric transmission and radiance for a number of wavelength channels collected by sensors distributed on locations all over the world.

## REFERENCES

1. N. Kolmogorov, The local structure of turbulence in an incompressible viscous fluid for very large Reynolds numbers, *C. R. (Dokl) Acad. Sci. USSR*. 30, 301–305 1941.
2. L. C. Andrews and R. L. Phillips, *Laser Beam Propagation through Random Media*, SPIE Optical Engineering Press, Bellingham, WA, 1998.
3. R. R. Beland, Propagation through atmospheric optical turbulence, in *The Infrared and Electro-Optical Systems Handbook*, F.G. Smith, (Ed.), SPIE Optical Engineering Press, Bellingham, WA, 1993, Vol. 2, Chapter 2.
4. G. Y. Jumper, H. M. Polchlopek, R. R. Beland, E. A. Murphy, P. Tracy, and K. Robinson, Balloon-borne measurements of atmospheric temperature fluctuations, 28th Plasmadynamics and Lasers Conference, AIAA-1997-2353, Atlanta, GA, June 23–25,

1997.

5. G. C. Valley, Isoplanatic degradation of tilt correction and short-term imaging systems, *Appl. Opt.* 19, 574–577, 1980.
6. R. J. Hill and S. F. Clifford, Modified spectrum of atmospheric temperature fluctuations and its application to optical propagation, *J. Opt. Soc. Am.* 68 (7), 892–899, 1978.
7. V. I. Tatarskii, *The Effect of the Turbulent Atmosphere on Wave Propagation* (Trans. for NOAA by Israel Program for Scientific Translations, Jerusalem, 1971).
8. D. L. Fried, Aperture averaging of scintillation, *J. Opt. Soc. Am.* 57 (2), 169–175, 1967.
9. J. H. Churnside, Aperture averaging of optical scintillations in the turbulent atmosphere, *Appl. Opt.* 30 (15), 1982–1994, 1991.
10. H. T. Yura and W. G. McKinley, Aperture averaging of scintillation for space-to-ground optical communication applications, *Appl. Opt.* 22, 1608–1610 1983.
11. G. Parry, Measurements of atmospheric turbulence-induced intensity fluctuations in a laser beam, *Opt. Acta* 28, 715–728, 1981.
12. E. Jakeman and P. N. Pusey, The significance of K-distribution in scattering experiments, *Physics. Rev. Lett.* 40, 546–550, 1978.
13. E. Jakeman, On the statistics of K-distributed noise, *J. Phys. A* 13, 31–48, 1980.
14. J. H. Churnside and R. J. Hill, Probability density of irradiance scintillations for strong path-integrated refractive turbulence, *J. Opt. Soc. Am. A* 4, 727–733, 1987.
15. J. H. Churnside and S. F. Clifford, Log-normal Rician probability-density function of optical scintillations in the turbulent atmosphere, *J. Opt. Soc. Am. A* 4, 1923–1930, 1987.
16. L. C. Andrews, R. Phillips, and C. Y. Hopen, *Laser Beam Scintillation with Applications*, SPIE Press, Bellingham, WA, 2001.
17. D. M. Strong, E. P. Magee, and G. B. Lamont, Implementation and test of wave optics code using parallel FFT algorithms, *Proc. SPIE* 4167, 34, 2001.

18. S. Coy, Choosing mesh spacings and mesh dimensions for wave optics simulation, *Proc. SPIE* 5894, 589405, 2005.
19. N. Roddier, Atmospheric wavefront simulation using Zernike polynomials, *Opt. Eng.* 29, 1174–1180, 1990.
20. D. L. Fried, Optical resolution through a randomly inhomogeneous medium, *J. Optic. Soc. Am.* 56, 1372–1379, 1966.
21. F. Roddier, The effects of atmospheric turbulence in optical astronomy, in *Progress in Optics XIX*, E. Wolf, (Ed.), North-Holland, New York, 1981.
22. J. W. Hardy, *Adaptive Optics for Astronomical Telescopes*, Oxford University Press, New York, 1998.
23. D. P. Greenwood and D. L. Fried, Power spectra requirements for wavefront compensative systems, *J. Opt. Soc. Am.* 66, 193–206, 1970.
24. R. K. Tyson, *Principles of Adaptive Optics*, 2nd edn., Academic, Boston, MA, 1998.
25. D. P. Greenwood, Bandwidth specifications for adaptive optics systems, *J. Opt. Soc. Am.* 67, 174–176, 1976.
26. D. L. Fried, Anisoplanatism in adaptive optics, *J. Opt. Soc. Am.* 72, 52–61, 1982.
27. L.C. Andrews; R. L. Phillips; R. J. Sasiela; R. R. Parenti, Strehl ratio and scintillation theory for uplink Gaussian-beam waves: beam wander effects, *Optical Engineering*, 45(7), (2006)
28. E. J. McCartney, *Optics of the Atmosphere*, Wiley, New York, 1976.
29. B.A. Bodhaine, B.A., N.B. Wood, E.G. Dutton, J.R. Slusser, On Rayleigh Optical Depth Calculations, *J. Atmos. Ocean. Tech.*, 16, 1854-1861, (1999).
30. W. E. K. Middleton, *Vision through the Atmosphere*, University of Toronto Press, Toronto, 1963.
31. H. C. van de Hulst, *Light Scattering by Small Particles*, Wiley, New York, 1957.

32. J. E. A. Selby and R. A. McClatchey, Atmospheric transmittance from 0.25 to 28.5  $\mu\text{m}$ : Computer code LOWTRAN 2, AFCRL-TR-72-0745, AD 763721, 1972.
33. A. Berk, L. S. Bernstein, and D. C. Robertson, MODTRAN: A moderate resolution model for LOWTRAN 7, GL-TR-89-0122, 1989.
34. A. Berk, F. Hawes Validation of MODTRAN 6 and its line-by-line algorithm, Journal of Quantitative Spectroscopy and Radiative Transfer, Volume 203, 542-556 , December 2017.
35. H. J. P. Smith, D. B. Dube, M. E. Gardner, S. A. Clough, F. X. Kneizys, and L. S. Rothman, FASCODE – fast atmospheric signature code (spectral transmission and radiance), AFGLTR-78-0081, ADA 057359, 1978.
36. Kasten, F.; Young, A. T., Revised optical air mass tables and approximation formula, *Appl. Opt.* **28**, 4735–4738, 1989.
37. F. S. Vetelino, B. Clare, K. Corbett, C. Young, K. Grant, and L. Andrews, Characterizing the propagation path in moderate to strong optical turbulence, *Appl. Opt.* 45, 3534–3543, 2006.
38. L. Wang, M. Schöck, G. Chanan, W. Skidmore, R. Blum, E. Bustos, S. Els, R. Riddle, J. Seguel, T. Travouillon, J. Vasquez, D. Walker, and P. Gillett, High-accuracy differential image motion monitor measurements for the thirty meter telescope site testing program, *Appl. Opt.* 46, 6460–6468, 2007.
39. <http://aeronet.gsfc.nasa.gov>.

